

NAT'L INST. OF STAND & TECH R.I.C.



A11104 045492



NATIONAL INSTITUTE OF STANDARDS &  
TECHNOLOGY  
Research Information Center  
Gaithersburg, MD 20899



A11102 140686

NBS  
PUBLICATIONS

NBSIR 82-2560

# NBS: Materials Measurements

U.S. DEPARTMENT OF COMMERCE  
National Bureau of Standards  
Washington, DC 20234

July 1982

Annual Report  
For the Period 1 April 1981 - 31 March 1982  
NASA Government Order H-27954B  
Properties of Electronic Materials



---

U.S. DEPARTMENT OF COMMERCE  
NATIONAL BUREAU OF STANDARDS

C-  
00  
56  
2-2560  
982  
. 2



NBSIR 82-2560

**NBS: MATERIALS MEASUREMENTS**

NATIONAL BUREAU  
OF STANDARDS  
LIBRARY

SEP 14 1982

101 1110  
C12  
OC100  
U56  
82-2560  
1982  
C.2

J. R. Manning

U.S. DEPARTMENT OF COMMERCE  
National Bureau of Standards  
Washington, DC 20234

July 1982

Annual Report  
For the Period 1 April 1981 - 31 March 1982  
NASA Government Order H-27954B  
Properties of Electronic Materials

**U.S. DEPARTMENT OF COMMERCE, Malcolm Baldrige, *Secretary***  
**NATIONAL BUREAU OF STANDARDS, Ernest Ambler, *Director***

1953

## TABLE OF CONTENTS

	<u>Page</u>
Summary . . . . .	1-3
Task 1 - SURFACE TENSIONS AND THEIR VARIATIONS WITH TEMPERATURE AND IMPURITIES S. C. Hardy and J. Fine. . . . .	5-24
Task 2 - CONVECTION DURING UNIDIRECTIONAL SOLIDIFICATION R. J. Schaefer, S. R. Coriell, R. G. Rehm and G. B. McFadden . . . . .	25-81
Task 3 - MEASUREMENT OF HIGH TEMPERATURE THERMOPHYSICAL PROPERTIES OF TUNGSTEN LIQUID AND SOLID D. W. Bonnell. . . . .	83-103



National Bureau of Standards  
Materials Measurements

Summary

This report describes NBS work for NASA in support of NASA's Materials Processing in Space Program under NASA Government Order H-27954B (Properties of Electronic Materials) covering the period April 1, 1981 to March 31, 1982. This work is directed toward measurement of materials properties important to the design and interpretation of space processing experiments and investigations of how the space environment may offer a unique opportunity for performing improved measurements and producing materials with improved properties.

This work is being carried out in three independent tasks:

Task 1. Surface Tensions and Their Variations with Temperature and Impurities

Task 2. Convection during Unidirectional Solidification

Task 3. Measurement of the High Temperature Thermophysical Properties of Tungsten Group Liquids and Solids

The results obtained for each task are given in detailed summaries in the body of the report. Emphasis in Tasks 1 and 2 is on how the reduced gravity obtained in space flight can affect convection and solidification processes. Emphasis on Task 3 is toward development of techniques for thermodynamic measurements on reactive materials, requiring levitation and containerless processing.

With the advent of the Space Shuttle, it may become feasible to exploit the unique microgravity environment of space flight to produce improved materials and improved measurements of important materials properties. In materials processing on earth, gravity frequently produces density-driven

convection, thereby causing liquids to be stirred as they solidify. This stirring disturbs the quiescent boundary layer at the solidifying interface, and can be very undesirable if nearly perfect crystals are required. For example, it creates interface instabilities, introduces segregation of components and produces crystal defects in the resulting solid material. These defects and inhomogeneities, which are particularly troublesome in electronic technology and other advanced technical applications, might be avoided in materials produced under microgravity conditions.

In Task 1, surface tension and surface segregation effects are being investigated to determine the possible influence of these surface effects on convection and solidification processes.

Even if gravity-driven convection is small, important convection effects still may arise from other sources. For example, convection can be produced by surface tension gradients. The variation of surface tension with temperature and composition often is not known, even for important technological materials such as silicon. NBS currently is making surface tension measurements on materials considered for space flight experiments. In addition, as part of this work segregation of impurities to the liquid surfaces is being investigated. Initial measurements were on gallium and gallium-tin alloys, selected as model materials useful for studying Marangoni convection and liquid metal surface effects at moderate temperatures.

The surface segregation studies that are being made include one of the first applications of Auger analysis techniques to liquid metals. These techniques have been very successful in producing informative results. Strong segregation effects were found in measurements on liquid metal surfaces. This segregation significantly affects surface tensions.

In Task 2, solutal convection, which results from simultaneous temperature and composition gradients, is being investigated both by theoretical calculations and by experiments. The experiments are designed to test the theories and provide quantitative data on convection processes on earth. Direct measurements of convection are being made during unidirectional solidification of transparent materials, particularly succinonitrile containing small amounts of ethanol. The theoretical calculations specifically include determinations of the effects a reduction in gravitational force will have on convection.

Interactions between temperature gradients and composition gradients can make it impossible to avoid solutal convection during materials processing on earth. Since this type of convection depends on gravity, its effects will be much less pronounced in space. NBS work is directed toward provision of measurements and development of models to define the conditions under which this type of convection will be important and determine how it can be avoided or controlled.

In Task 3, assistance is being provided to a joint project involving investigators from Rice University (Prof. J. Margrave) and General Electric Co. (Dr. R. T. Frost) in which a General Electric electromagnetic levitation facility is being applied to develop levitation/drop calorimetry techniques and determine their possibilities and limitations. Measurements of the specific heat of liquid tungsten uncontaminated by reaction with container walls currently is being pursued in earth's gravity experiments. Several aspects of the techniques being developed should also be useful for space flight experiments.



Task 1

The Measurement of Surface Tensions and  
Their Variation with Temperature and Concentration

S. C. Hardy  
Metallurgy Division  
Center for Materials Science

and

J. Fine  
Surface Science Division  
Center for Chemical Physics

Summary

A series of Ga-Sn liquid alloys has been studied by Auger electron spectroscopy. The Sn was found to be strongly adsorbed at the surface. Calculations of surface concentrations from the Auger measurements are shown to be substantially in agreement with surface concentrations deduced from thermodynamic data. This result supports the monolayer model of surface adsorption for the Ga-Sn system.

## Introduction

Components of a bulk liquid phase which have low intrinsic surface tensions will preferentially segregate at free surfaces. Although the thermodynamics of this surface adsorption phenomenon was developed by Gibbs over a hundred years ago, many questions remain unanswered about details of the process such as the distribution of the adsorbed species in the surface region and the interactions between coadsorbing species. Adsorption can in some situations result in large surface tension gradients which generate fluid flow. These "Marangoni" flows are the dominant type in low gravity.

The study of adsorption at liquid surfaces is currently an active field of research with a long history. There have been almost no applications of modern surface analysis techniques to liquids, however, although there would appear to be no fundamental impediment to such studies for low vapor pressure and melting point materials. Perhaps the oldest and most widely used of the new surface analysis techniques is Auger electron spectroscopy, yet we know of only two previous applications to liquids [1,2]. Both of these were attempts to measure the surface segregation in binary alloy systems. A related technique, electron energy loss spectroscopy, has recently been used to study the oxidation of liquid Sn surfaces [3].

During the past contract year, we have been studying surface segregation in liquid Ga-Sn alloys using Auger spectroscopy. This system was chosen for study because of the low vapor pressures and melting points of its components and because surface tension measurements in the literature indicated a strong adsorption of Sn at the interface [4]. Furthermore, the combination of Ga and Sn is interesting from a surface characterization point of view since Auger electrons cover a wide energy range for this system: Ga has prominent lines at 55 e.v. and 1070 e.v. and Sn at 430 e.v. The escape

depth for the Auger electrons varies from approximately one to six monolayers over this energy range. Thus the liquid composition can be sampled to different depths into the bulk. The primary objective of this work is to see if the surface concentrations of the alloy components deduced from the Auger measurements are in agreement with those deduced from the surface tension data. Such agreement would support the results of the Auger determination of surface concentrations in other alloy systems for which good thermodynamic measurements are unavailable.

### Experimental

A detailed description of the equipment we use has been given in a previous report [5]. Briefly, the Auger spectrometer is a conventional single-pass cylindrical mirror analyzer system (CMA) with a coaxial electron gun. The CMA is mounted vertically so that it can be focused on the top surface of a sessile drop sample. The electron beam used to excite the Auger electrons has a diameter of about 3  $\mu\text{m}$  and can be rastered to form a video image of the drop surface. Auger data is acquired in an analog mode using first derivative spectral display. The base of the sessile drop is contained in an alumina cup which is clamped to a simple hot stage mounted on the rotatable platform of a horizontal manipulator. Four drops are accommodated by the hot stage and can be successively brought into position for analysis by rotation. Electrical contact to the drops is made with fine W wire probes which are insulated from the hot stage. The temperature is monitored by a chromel-alumel thermocouple spot welded to the top of the hot stage. The drop temperature was compared with the temperature of the hot stage by inserting a W-Rh thermocouple directly into a drop in a calibration experiment. In subsequent work drop temperatures were determined from the reading of the hot stage thermocouple using these calibration measurements.

Sessile drops are formed by placing pieces of high purity Sn and Ga of the desired weight in the cups and melting them after evacuation of the system. The surfaces of the drops are covered initially by oxide layers with high carbon contents. This overlayer of impurities is removed from the liquid surface by sputtering with argon ions [6]. Although a few residual islands of impurities may persist after sputtering, the surface area under analysis is clean, at least to the sensitivity of Auger spectroscopy. For accurate measurements of surface concentrations it is necessary that the surface be impurity free since the Auger electron intensities can be significantly reduced by fractional monolayer coverages.

In our initial measurements, pure Ga and pure Sn samples were studied in order to establish the relative magnitudes of the three prominent Auger lines of this alloy system as a function of spectrometer variables. In subsequent work one of the cups always contained a pure sample of either Ga or Sn. The spectrum of this standard was recorded before and after each alloy drop spectrum to allow normalization of the Auger line intensities.

The Sn Auger spectrum, in addition to the strong line at 430 e.v., contains a broad, weak, line which overlaps the low energy Ga line at 55 e.v. By superposition of spectra from pure Ga and Sn it was estimated that, in an alloy sample, this low energy feature of the Sn Auger spectrum would increase the apparent amplitude of the 55 e.v. Ga line by about 1.9% of the amplitude of the observed 430 e.v. line for that alloy. Thus, as a first approximation, we have corrected the 55 e.v. line by subtracting this amount, i.e.,  $I'_{Ga_1} = I_{Ga_1}^0 - .019 I_{Sn}^0$ . Here  $I_{Ga_1}^0$  and  $I_{Sn}^0$  are the measured peak-to-peak line amplitudes at 55 e.v. and 430 e.v. and  $I'_{Ga_1}$  is the adjusted amplitude. The correction to the low energy Ga line amplitude becomes important as the Sn concentration increases. For  $X_{Sn}^B = .70$ , where  $X_{Sn}^B$  is

the bulk atomic fraction,  $.019 I_{\text{Sn}}^0 = .43 I_{\text{Ga}}^0$ . At higher Sn concentration, the low energy Sn feature obscures the peaks of the Ga line making measurement impossible. Thus, the determination of the amplitude of the 55 e.v. Ga line becomes increasingly difficult as the bulk Sn concentration increases and we anticipate a consequent loss of accuracy. A more elaborate correction procedure which considered the escape depth of the Auger electrons and the distribution of Sn near the surface gave essentially the same results as this simple approach.

In Figure 1 we show the results of the Auger measurements. The observed peak-to-peak line amplitudes have been normalized using the observed amplitudes of the corresponding lines in a pure unalloyed specimen under identical conditions. The amplitude of the 55 e.v. Ga line has been corrected using the procedure described above. This is the basic experimental data which will be analyzed subsequently.

### Results and Discussion

#### a. Thermodynamic Data

We wish to compare the surface concentrations estimated from the Auger measurements with the concentrations derived from surface tension measurements. This latter analysis is made basically with the Gibbs adsorption equation. The relative adsorption  $\Gamma_A^{(B)}$  of component A with respect to component B at the interface is given by

$$\Gamma_A^{(B)} = - \frac{1}{RT} \left( \frac{\partial \gamma}{\partial \ln a_A} \right)_{T, a_B} \quad (1)$$

where  $a$  is the thermodynamic activity,  $\gamma$  is the surface tension,  $T$  is the absolute temperature, and  $R$  is the gas constant. To calculate the relative

adsorption the surface tension is plotted as a function of  $\ln a_A$  and the slope is measured along the curve. In Figure 2 we show such a plot for Ga-Sn alloys at  $T = 623$  K. This data is from the Russian work [4] and is in general agreement with other data in the literature and with measurements in our laboratory at several concentrations. Although the slope determination is somewhat uncertain at low concentrations where  $|\ln a_{\text{Sn}}|$  is large, it is well defined over most of the composition range. There is an anomalous increase in surface tension near  $\ln a_{\text{Sn}} = -0.55$ . This corresponds to a bulk concentration of Sn of 0.6 atomic fraction. Similar features are seen in surface tension measurements in other alloy systems and are generally not understood. We will not attempt to calculate adsorption near this anomaly, but will simply extrapolate through this region. The adsorptions calculated from the slope in Figure 2 give the number of excess Sn atoms near the liquid vapor interface. If these are considered to be confined to a single layer so that atomic fractions in the monolayer,  $X_{\text{Sn}}^{\text{S}}$  and  $X_{\text{Ga}}^{\text{S}}$ , can be defined, the following expression for the concentration of Sn at the surface is obtained [7]:

$$X_{\text{Sn}}^{\text{S}} = \frac{X_{\text{Sn}}^{\text{B}} + (1 - X_{\text{Sn}}^{\text{B}}) \Gamma_{\text{Sn}}^{(\text{Ga})} \alpha_{\text{Ga}}}{1 + (1 - X_{\text{Sn}}^{\text{B}}) \Gamma_{\text{Sn}}^{(\text{Ga})} (\alpha_{\text{Ga}} - \alpha_{\text{Sn}})} \quad (2)$$

Here  $\alpha_{\text{Ga}}$  and  $\alpha_{\text{Sn}}$  are the atomic areas of pure Ga and Sn respectively and  $X_{\text{Sn}}^{\text{B}}$  is the bulk concentration of Sn (atomic fraction). The surface concentration of Sn calculated using this monolayer model and the data shown in Figure 2 is shown in Figure 3. The Sn is seen to be strongly adsorbed attaining a concentration at the surface of about 0.6 at a bulk concentration of 0.1.

#### b. Surface Concentrations from Auger Data

The determination of surface concentrations from measurements of Auger line amplitudes may be carried out at several levels of approximation. In a

first approximation this is often done by equating the surface concentration with the normalized line amplitudes, i.e.,  $X_{\text{Sn}}^{\text{S}} = I_{\text{Sn}}^0 / I_{\text{Sn}}^{\infty}$  where  $I_{\text{Sn}}^{\infty}$  is the peak-to-peak line amplitude measured for pure Sn. Surface concentrations calculated in this approximation from our measurements are shown in Figure 4 along with the concentrations deduced from thermodynamics shown previously in Figure 3. We have converted the surface concentrations of Ga calculated from the Ga Auger data to Sn concentrations by computing  $X_{\text{Sn}}^{\text{S}} = 1 - X_{\text{Ga}}^{\text{S}} = 1 - I_{\text{Ga}}^0 / I_{\text{Ga}}^{\infty}$ . The data shown in Figure 4 illustrate that surface concentrations calculated in this approximation become inaccurate as the electron energy increases. This deterioration in the approximation comes about because Auger electrons of higher energy escape the sample from significant depths and add a bulk component to the detected signal which obscures the fraction originating in the surface layer. Thus, it is necessary to account for this bulk contribution in order to measure surface concentrations.

The Auger electron current from a component A of an alloy AB may be written as:

$$I_{\text{A}}^{\text{AB}} = g I_{\text{p}} \sigma_{\text{A}} \gamma_{\text{A}} R_{\text{AB}} \int_0^{\infty} C_{\text{A}}(z) e^{(-z/\lambda \cos\theta)} dz \quad (3)$$

where  $g$  is a geometrical factor,  $I_{\text{p}}$  is the primary beam current,  $\sigma_{\text{A}}$  is the ionization cross section,  $\gamma_{\text{A}}$  is a relaxation coefficient,  $R_{\text{AB}}$  is the back-scattering factor,  $C_{\text{A}}(z)$  is the concentration of A atoms/cm<sup>3</sup>,  $z$  is the distance from the surface in units of number of monolayers, and  $\lambda$  is the inelastic mean free path for electrons in units of number of monolayers. The  $\cos\theta$  term is dependent on the geometry of the analyzer and for our instrument is 0.74. If the concentration  $C_{\text{A}}(z)$  is considered to be uniform in the bulk up to a surface layer of a different composition, an integration of the above equation and the analogous equation for pure A gives:

$$\frac{I_A^{AB}}{I_A^\infty} = \frac{R_{AB}}{R_A} \frac{\ell_{AB}}{\ell_A} \frac{N_{AB}}{N_A} \left\{ X_A^S \left[ 1 - \exp\left(-\frac{1}{\ell_{AB}}\right) \right] + X_A^B \exp\left(-\frac{1}{\ell_{AB}}\right) \right\} \quad (4)$$

where  $N$  is the atomic density (atoms/cm<sup>3</sup>),  $\ell = \lambda \cos\theta$ , and  $X_A^S$  and  $X_A^B$  are the atomic fractions of A in the surface layer and in the bulk respectively.

The subscripts A and AB indicate pure material and alloy. Solving for the surface concentration,

$$X_A^S = \frac{I_A^{AB}/F_A I_A^\infty - X_A^B e^{-1/\ell_{AB}}}{1 - e^{-1/\ell_{AB}}}, \quad (5)$$

where we have written  $F_A = \frac{R_{AB}}{R_A} \frac{\ell_{AB}}{\ell_A} \frac{N_{AB}}{N_A}$ . Values for the atomic density required to evaluate equation (5) can be calculated from the mass density.

The backscattering factor and Auger electron mean free paths, however, are not so well known. The backscattering factor  $R$  describes the Auger electrons which are generated by the backscattered primary beam.  $R$  is a function of primary beam energy  $E_p$ , Auger electron energy  $E$ , and the matrix. We have derived  $R$  values appropriate to Sn and Ga from recent Monte Carlo calculations [8]. This was done by plotting the  $R$  values found in the calculation as a function of reduced energy,  $U = E_p/E$ , for  $Z = 31$  (Ga) and  $Z = 50$  (Zn). The  $R$  values appropriate to our  $U$  could then be interpolated from the graphs. In Table 1 we give the values of  $R$  for Ga and Sn obtained in this way. For the alloys, the backscattering factor was assumed to be directly proportional to the bulk concentration, i.e.,

$$R_{Ga,Sn} = R_{Ga} + X_{Sn}^B [R_{Sn} - R_{Ga}] \quad (6)$$

The critical factor in equation 5 is the exponential function of the inelastic mean free path. Although there have been several measurements of this quantity for Sn [9,10], we do not know of any measurements for Ga. The measurement of inelastic mean free paths is difficult and published values are often of uncertain accuracy. We will, therefore, calculate inelastic mean free paths for Ga and Sn using the recently developed theory of Szajman et al. [11] which seems to predict  $\lambda$  accurately for aluminum, a metal electronically similar to Ga and Sn. In Figure 5 we show the predicted  $\lambda$  values for the case of Ga and Sn using this theory; we also show the prediction of the Seah and Dench [12] empirical equation for Sn and the values measured experimentally at two energies [9,10]. The data point at 430 e.v. was taken from Seah's work in which he deposited Sn on an Fe substrate and measured the change in Auger signal with film thickness. We have adjusted his data using backscattering factors for Sn and Fe calculated as discussed earlier. This reduced his estimate of  $\lambda$  by about 40% and brings his measurement into good agreement with the predictions of theory. The Szajman theory must become inaccurate at low energies because it does not predict the minimum in the  $\lambda$  vs. E curve at around 100 e.v. with the strong rise at very low energies (< 10 e.v.) shown in the Seah and Dench compilation [12]. Lacking any rigorous method for correcting the Szajman theory in this region, we will simply add the empirically determined  $538/E^2$  term used by Seah and Dench. In Table 2 we list the calculated  $\lambda$  values which we will use subsequently to evaluate the Auger data. The  $\lambda$  values for Ga and Sn are nearly the same so we will use their average for all alloy compositions.

#### c. Comparison of Auger and Thermodynamic Data

In Figure 6 we compare the surface concentrations calculated from thermodynamics (curve) with the concentrations of Sn determined using

the normalized Auger amplitudes, the backscattering factors, and the inelastic mean free paths of Tables 1 and 2 as inputs to equation (5). The filled circles are surface concentration obtained for the 430 e.v. Sn line. The Ga surface concentration  $X_{Ga}^S$  was also calculated using the 55 e.v. Auger data. This was then converted to a surface concentration of Sn, i.e.,  $X_{Sn}^S = 1 - X_{Ga}^S$ . This data is shown in Figure 6 as open circles. In Figure 7 we have expanded the low concentration range of Figure 6 to better display the data. The one point which lies significantly off the curve determined from thermodynamics is believed to be in error due to an impurity island momentarily drifting into the electron beam during analysis. The deviation of the two sets of data at high concentrations may indicate an inaccuracy in the thermodynamic analysis rather than the Auger data. This deviation occurs in the region containing the anomalous rise in the surface tension which made the determination of the relative adsorption difficult. A loss in accuracy in the calculation of the surface concentration using the Sn data at 430 e.v. is to be expected at high bulk concentrations of Sn because the Auger signal is predominantly from the bulk in this case. The soft Auger electron data at 55 e.v. is increasingly uncertain at high Sn concentrations because the correction discussed earlier becomes large. The standard deviation of  $X_{Sn}^S$  determined by Auger from the thermodynamically determined  $X_{Sn}^S$  is about 7% for the low energy electrons; this increases to 11% for the 430 e.v. data. The disagreement is surprisingly small considering the uncertainty of the factors entering into the evaluation. Better agreement with the thermodynamic  $X_{Sn}^S$  could be obtained for the 430 e.v. measurement if a smaller  $\lambda$  were assumed.

## Summary

The analysis of the Auger line amplitudes for Ga-Sn alloys at 350 °C shows that the Sn is strongly adsorbed at the surface. Using calculated values for the inelastic mean free path and the backscattering factors for the Auger electrons permits the determination of surface concentrations which are in good agreement with the concentrations derived thermodynamically from surface tension measurements. This agreement supports the validity of the monolayer model which considers all the surface segregated Sn atoms to be in the top layer. The approach used here to calculate surface concentrations from Auger measurements is generally useful for metals which have a relatively soft Auger electron.

Table 1. The backscattering factors for Ga and Sn interpolated from the calculations of Shimura and Shimizu [8].

E (e.v.)	$R_{\text{Ga}}$	$R_{\text{Sn}}$
55	1.94	2.15
430	1.60	1.74
1070	1.34	1.44

Table 2. The inelastic mean free paths for Ga and Sn in monolayers calculated using the equation of Szajman and Leckey [11].

E (e.v)	$\lambda_{\text{Ga}}$ (monolayers)	$\lambda_{\text{Sn}}$ (monolayers)	$538/E^2$ (monolayers)	$\lambda_{\text{avg.}}$ (monolayers)
55	.92	.90	.18	1.09
430	4.27	4.20	0	4.23
1070	8.99	8.87	0	8.93

## References

1. S. Berglund and G. A. Somorjai, J. Chem. Phys. 59, 5537 (1973).
2. P. Laty, J. C. Joud and P. Desre, Surface Sci. 104, 105 (1981).
3. J. D. Verhoeven, M. A. Noack and A. J. Bevolo, in the Proceedings of the Materials Processing Research in the Reduced Gravity Environment of Space Symposium, Guy E. Rindone, Chairman, Boston, 1981.
4. A. G. Nalgiev and K. I. Ibragimov, Zh. Fiz. Kim. 48, 1289 (1974).
5. NBS: Materials Measurements, NBSIR 81-2295, June 1981.
6. J. Fine, S. C. Hardy and T. D. Andreadis, J. of Vacuum Sci. & Tech. 18, 1310 (1981).
7. M. Brunet, J. C. Joud, N. Eustathopoulos and P. Desre, J. Less-Common Metals 51, 69 (1977).
8. S. Ichimura and R. Shimizu, Surface Sci. 112, 386 (1981).
9. M. P. Seah, Surface Sci. 40, 595 (1973).
10. P. Cadman and G. M. Gossedge, J. of Elect. Spect. and Related Phenom. 18, 161 (1980).
11. J. Szajman and R. C. G. Leckey, J. of Elect. Spect. and Related Phenom. 23, 83 (1981).
12. M. P. Seah and W. A. Dench, Surface Interface Anal. 1, 2 (1979).

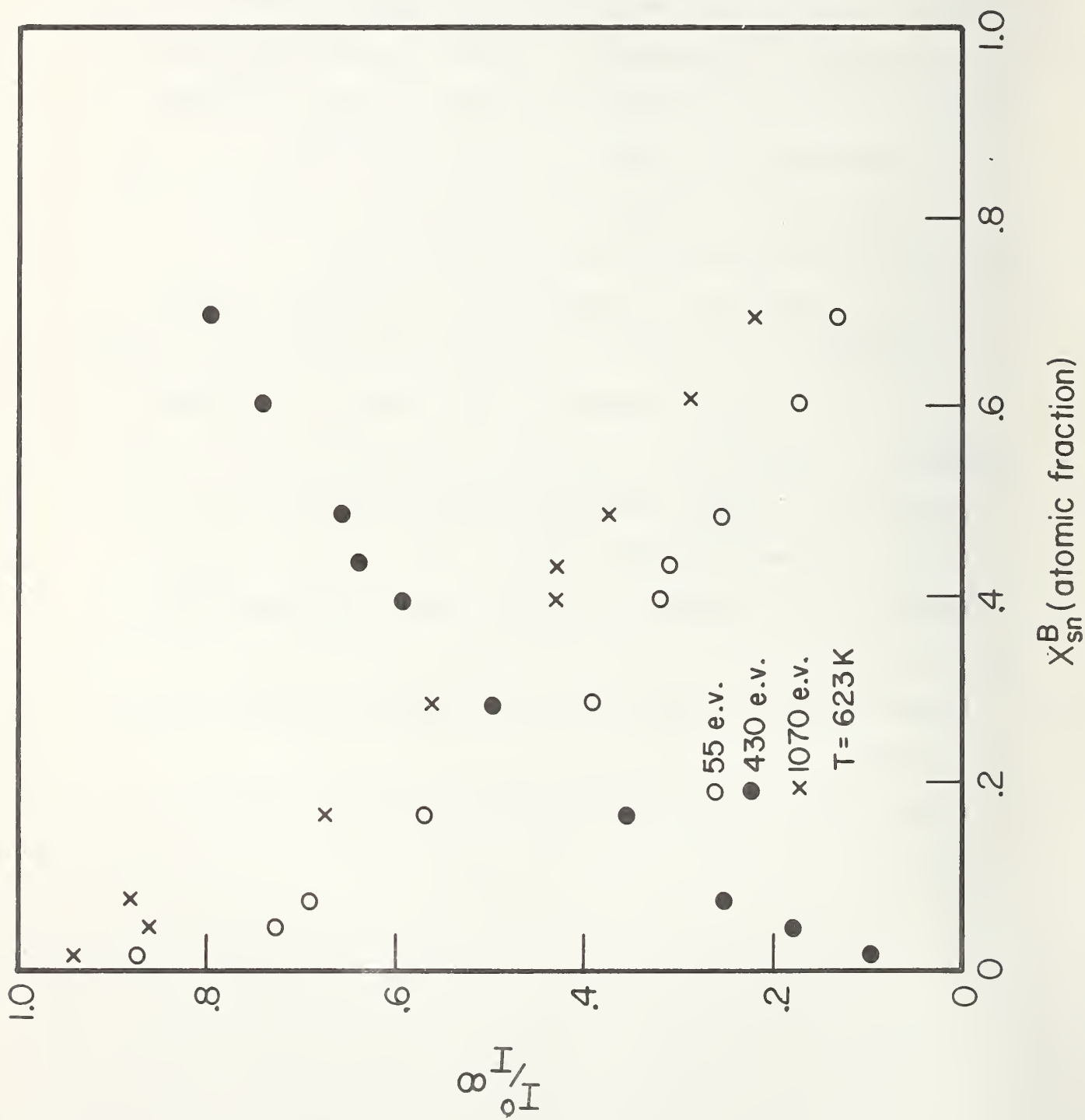


Fig. 1. The normalized peak-to-peak Auger line amplitude  $I^0/I^\infty$  as a function of bulk Sn concentration  $X_{Sn}^B$ .  $I^0$  is the amplitude of the line measured

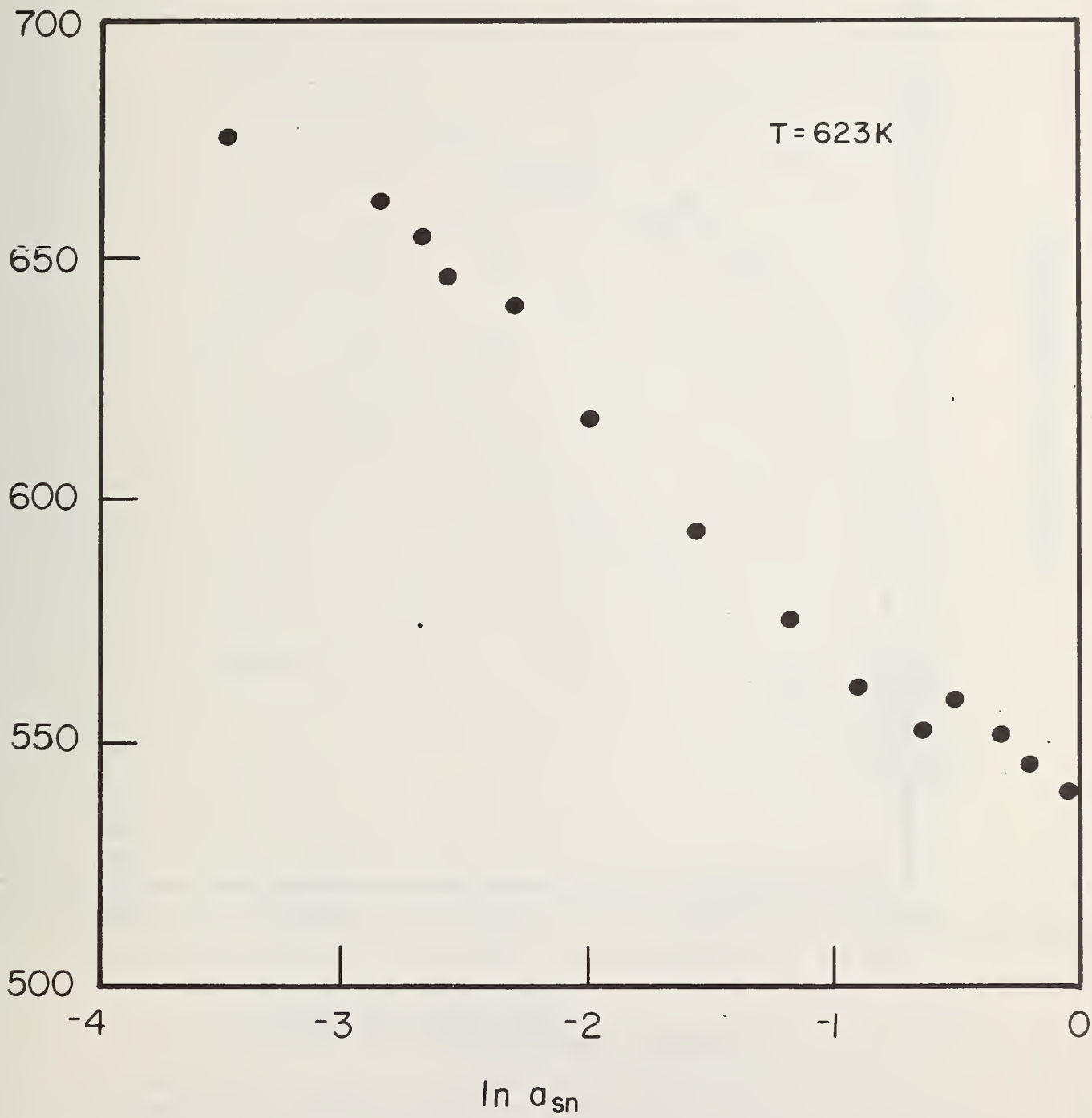


Fig. 2. The surface tension of Ga-Sn alloys  $\gamma$ <sup>[4]</sup> as a function of the log of the thermodynamic activity  $a_{\text{Sn}}$ .

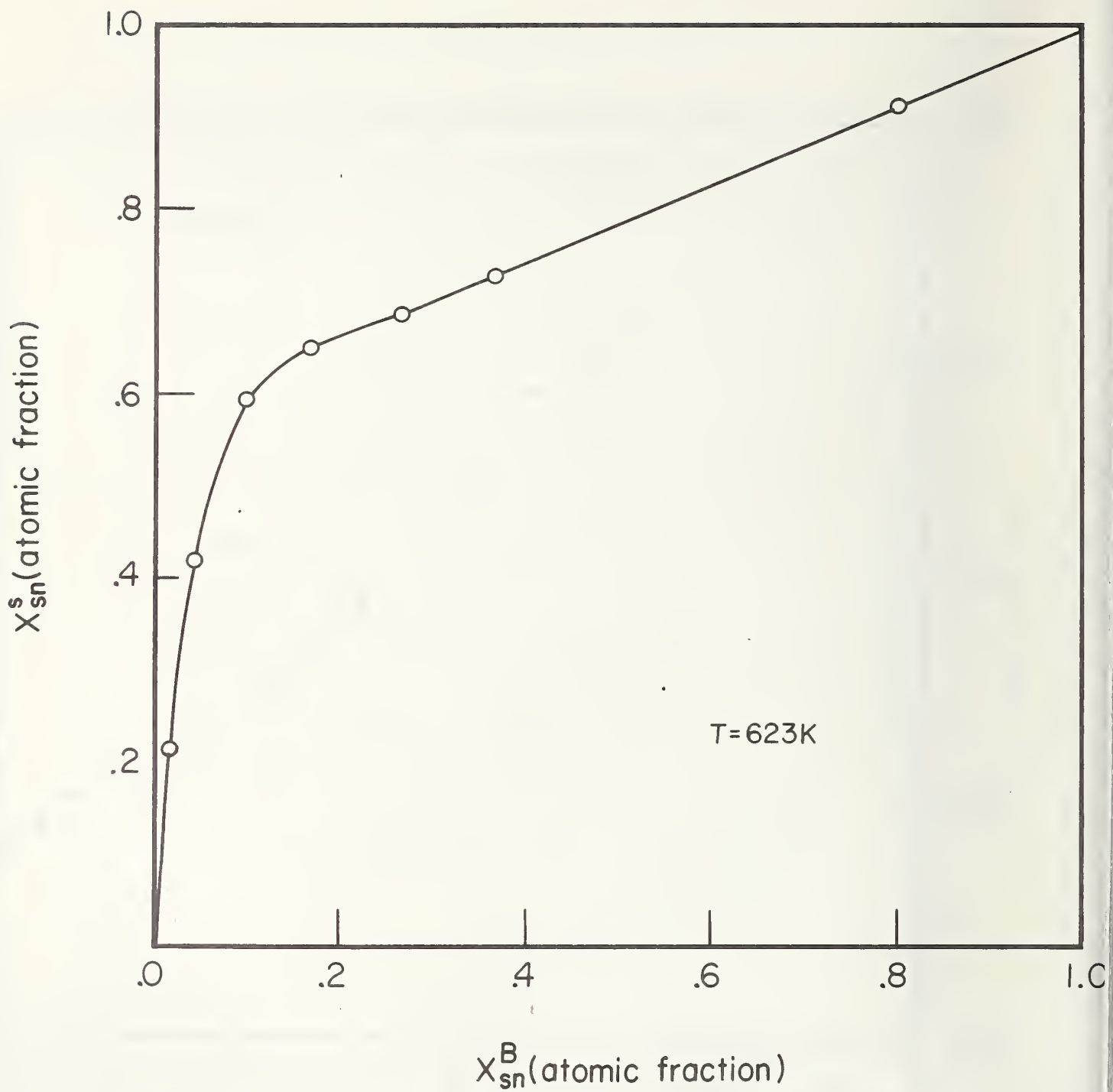


Fig. 3. The surface concentration of tin  $X_{Sn}^S$  as a function of the bulk concentration  $X_{Sn}^B$  determined from the surface tension data and equation 2.

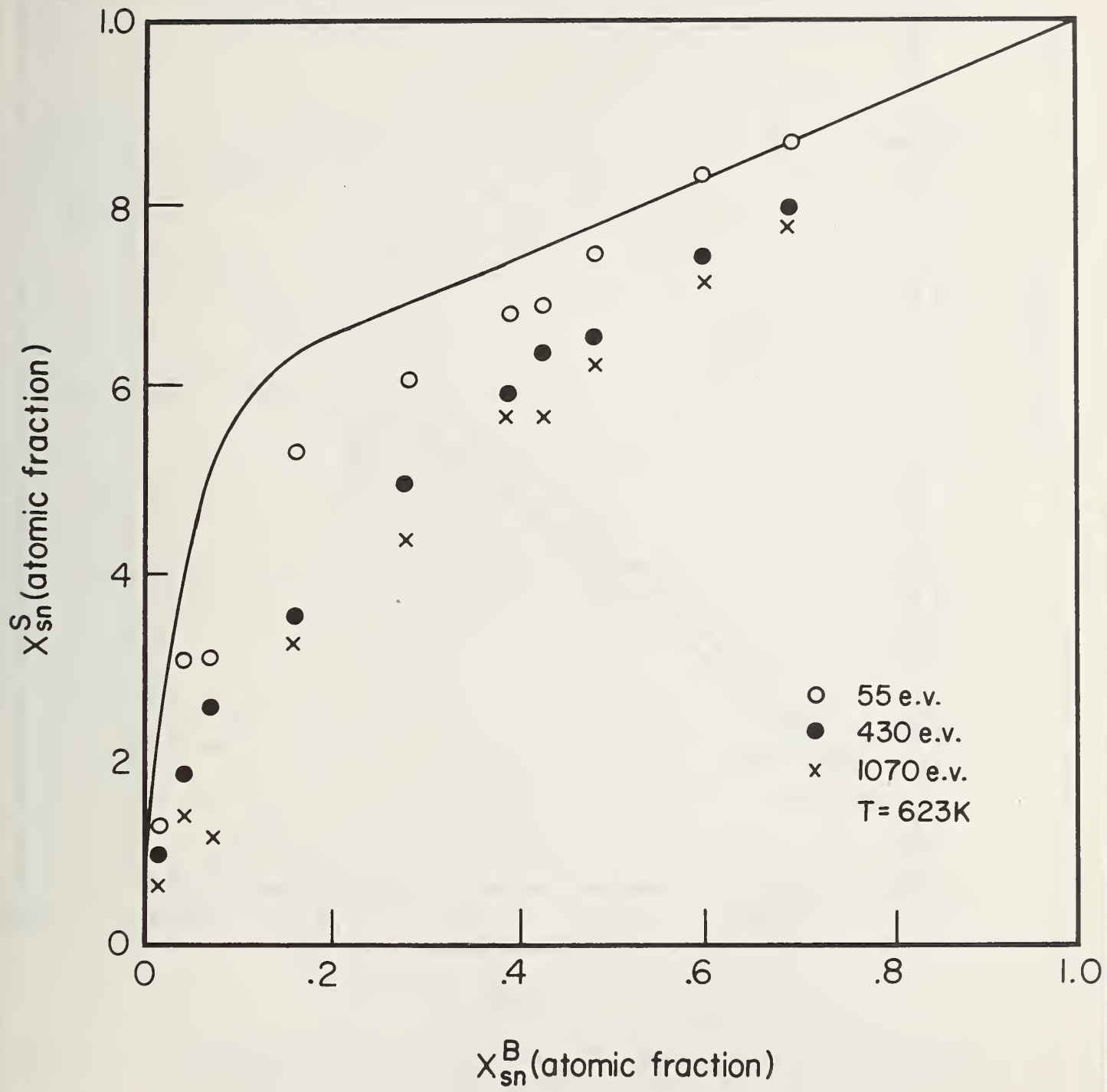


Fig. 4. Comparison of  $X_{Sn}^S$  shown in figure 3 with  $X_{Sn}^S$  values calculated from the Auger measurements in the approximation  $X_{Sn}^S = I_{Sn}^0 / I_{Sn}^\infty$ .

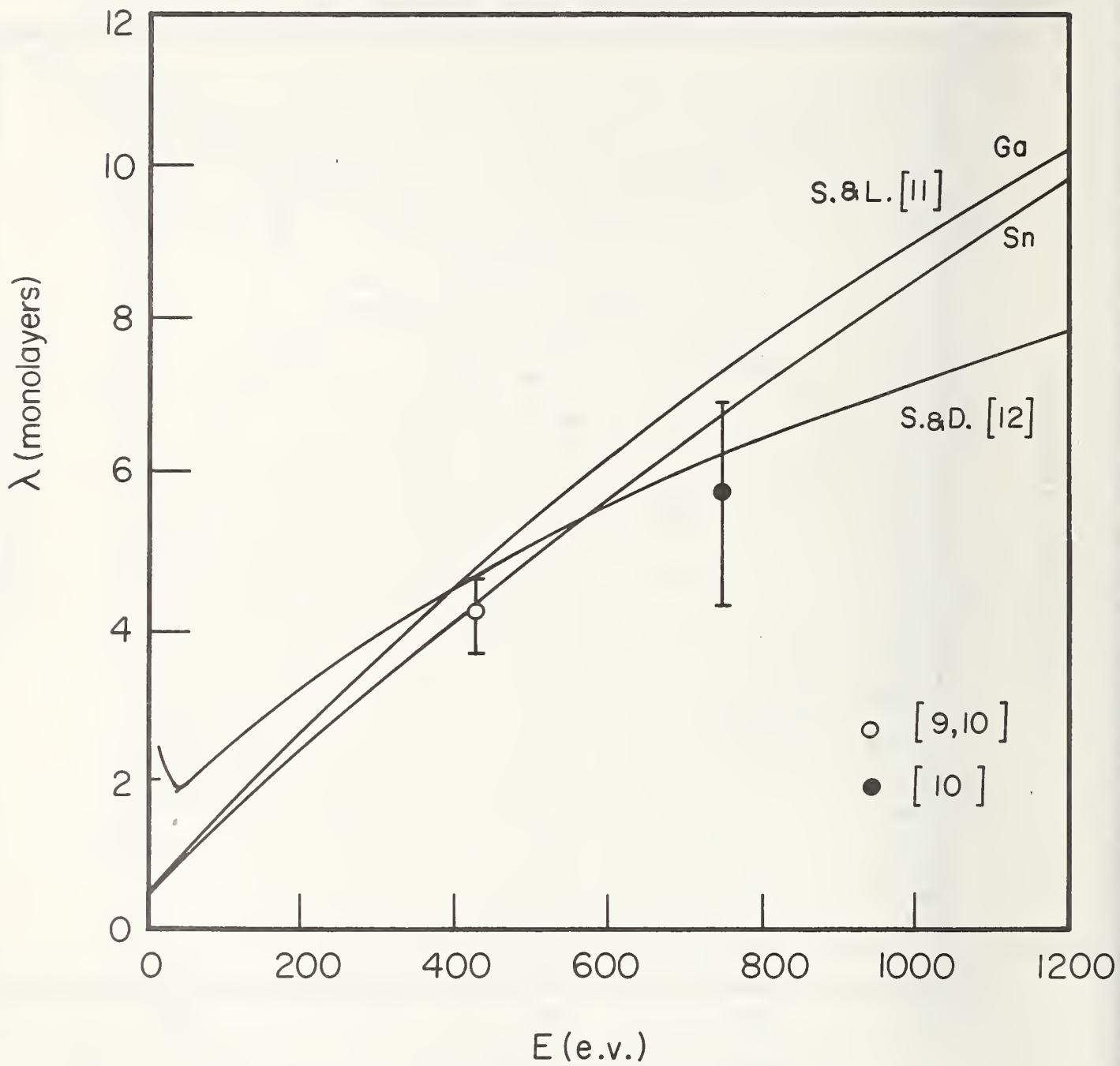


Fig. 5. The inelastic mean free path for electrons  $\lambda$  as a function of electron energy  $E$ .

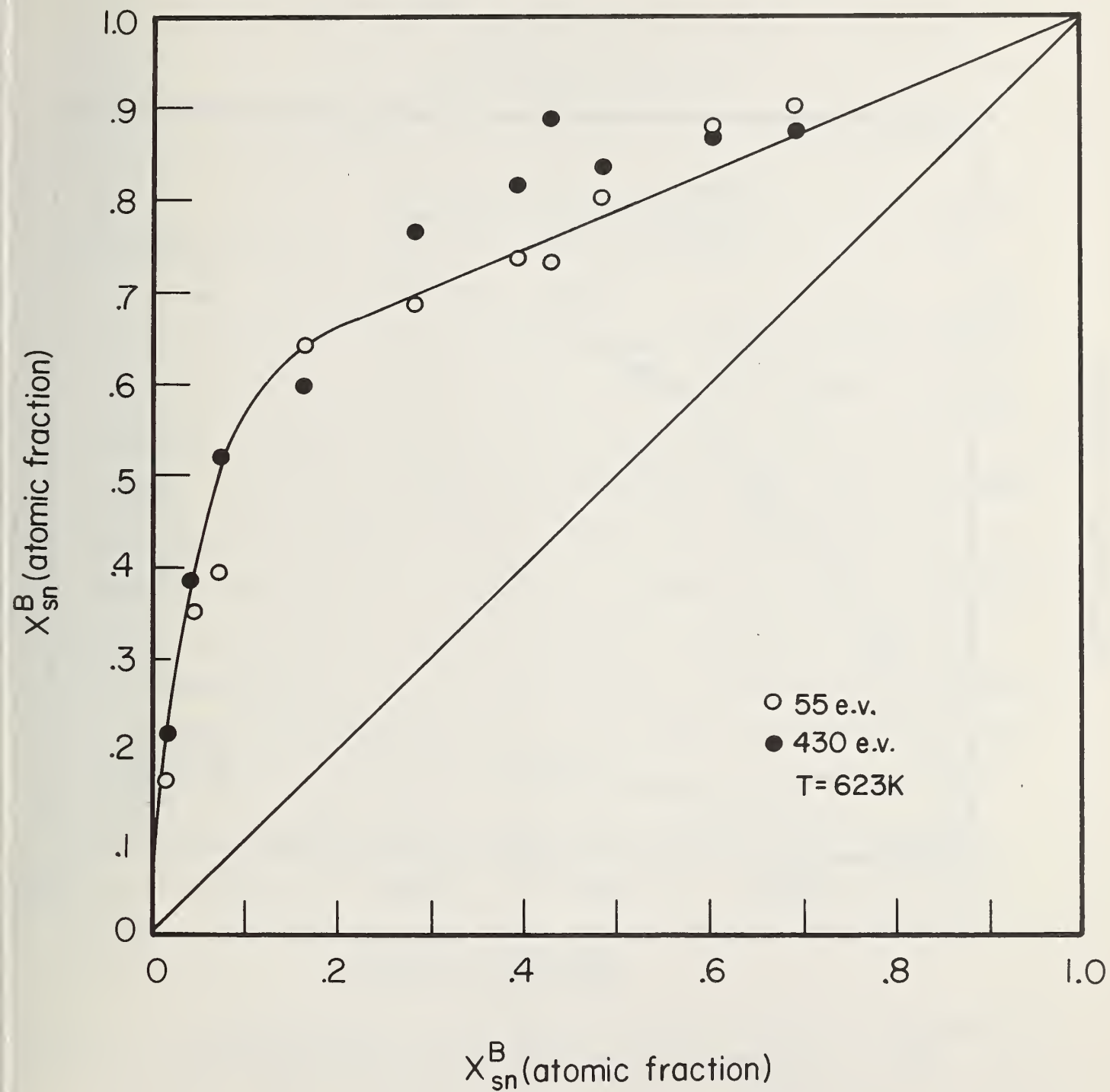


Fig. 6. The surface concentration  $X_{Sn}^S$  calculated using equation 5 as a function of the bulk concentration  $X_{Sn}^B$ . The curve is the thermodynamically determined concentration variation shown in figure 3.

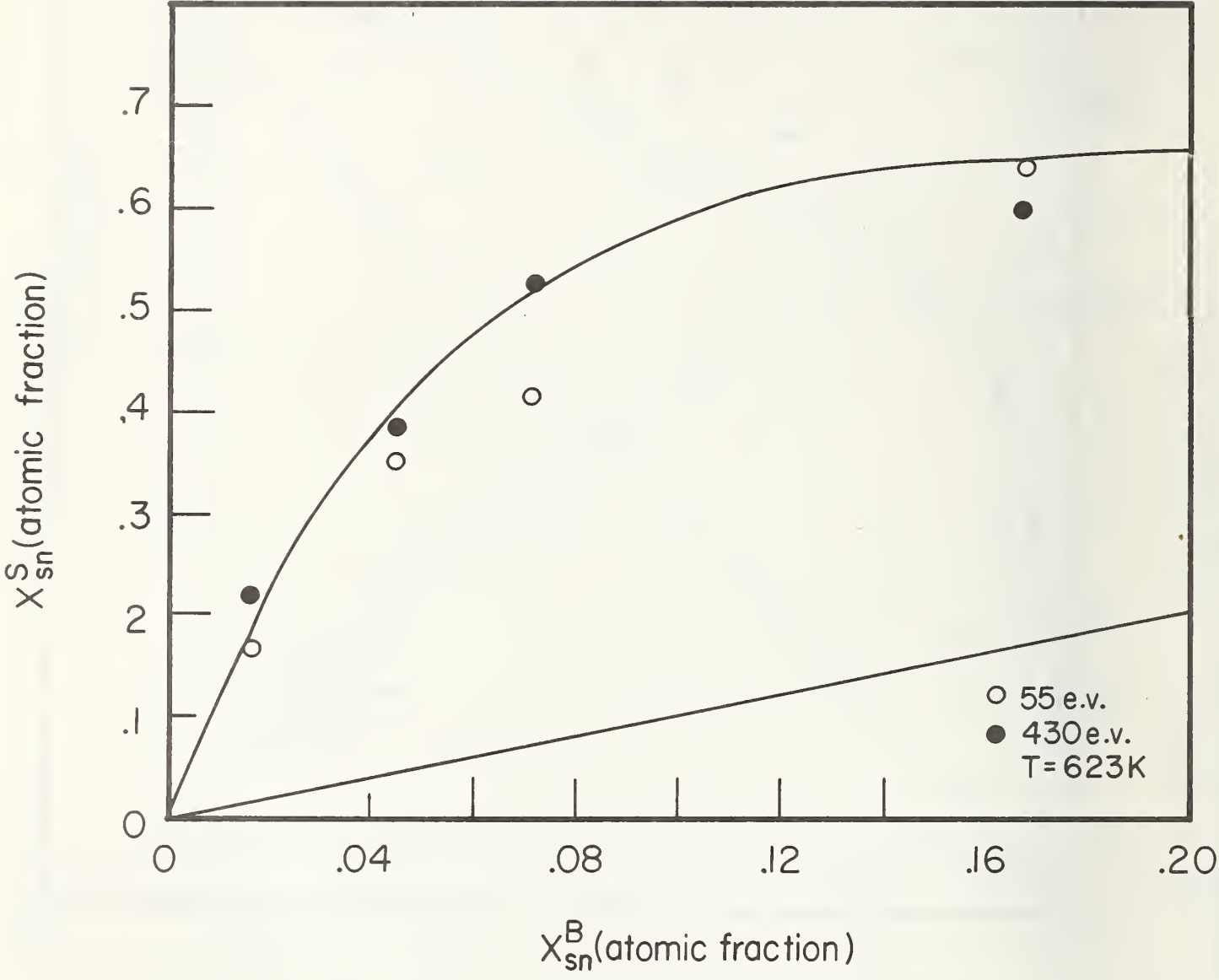


Fig. 7. An expanded display of the surface concentration  $X_{Sn}^S$  at low values of  $X_{Sn}^B$ .

## Convection During Unidirectional Solidification

R. J. Schaefer and S. R. Coriell  
Metallurgy Division  
Center for Materials Science

and

R. G. Rehm and G. B. McFadden  
Mathematical Analysis Division  
Center for Applied Mathematics

## Summary

A theoretical model is presented of double diffusive convection induced in a binary liquid during crystal growth. The interface between the liquid and solid is assumed to remain flat and the crystal is taken to grow at constant velocity. The nonlinear partial differential equations of fluid flow together with equations for temperature and concentration are solved numerically. The numerical methods and some checks used to ascertain the validity of the methods are briefly described, and sample solutions are presented and discussed.

During directional solidification of pure or ethanol-doped succinonitrile, it was found that some convection of purely thermal origin was always present. In the ethanol-doped sample this convection leads to the development of a macroscopic depression in the solid-liquid interface, which subsequently becomes the site of a localized cellular structure. An overall cellular interface appears at conditions close to those predicted for interfacial instability.

In collaboration with M. E. Glicksman and J. I. Mickalonis of Rensselaer Polytechnic Institute, the stability of the flow between two vertical, infinite, rigid, coaxial cylinders held at different temperatures is analyzed by linear stability theory. When the rigid outer cylinder-fluid interface is replaced by a crystal-melt interface which can change shape, new "coupled modes" of

instability occur at lower values of the Grashof number. These calculations were motivated by and are in general agreement with recent experiments at Rensselaer Polytechnic Institute on succinonitrile.

## Introduction

The general aim of this task is the theoretical and experimental study of the fluid flow and solute segregation which occur during solidification. The nature of the fluid flow, its effect on the shape of the crystal-melt interface and on the resulting distribution of solutes is examined. In particular, the role of solutal convection (gravity driven flow due to solute gradients) during the vertical directional solidification of a binary alloy is considered both theoretically and experimentally.

We present a discussion of the theoretical work first and then a description of the experiments: each section can be read independently. The theoretical section describes numerical methods for solving the fluid dynamical, temperature, and concentration equations appropriate to directional solidification of a binary alloy. Some example results of these calculations are given. The experimental section describes the fluid flow and crystal-melt interface shapes observed during the directional solidification of succinonitrile containing small additions of ethanol.

In an appendix, we describe a linear stability analysis relevant to experimental work being conducted at Rensselaer Polytechnic Institute. As described in the Appendix an interface instability occurs under conditions for which in the absence of fluid flow, the crystal-melt interface would be morphologically stable.

The Mathematical Model of Solutal Convection

The problem considered is that of natural convection induced during unidirectional solidification of a binary alloy. The crystal is grown vertically upwards at constant velocity  $V$  from a binary liquid with a concentration  $C$  of solute [1]. Figure 1a shows a schematic diagram of the configuration.

The initial state is one in which the solid rejects or preferentially incorporates solute at the interface giving rise to an exponential concentration gradient of solute ahead of the interface with a decay distance  $D/V$  as shown in Figure 1b. Also, an exponential temperature gradient exists in the liquid with a decay distance  $\kappa/V$  and in the solid with characteristic distance  $\kappa_S/V$ . Here,  $\kappa$  and  $\kappa_S$  are the thermal diffusivities in the liquid and solid respectively and  $D$  is the diffusion coefficient for solute.

A large solute concentration gradient will induce natural, or buoyant convection, often called double diffusive convection [2], if the solute rejected is lighter than the solvent or a preferentially incorporated solute is heavier than the solvent. The temperature gradient, on the other hand, is a stabilizing influence since the colder fluid will stably reside near the interface. It is the double diffusive convection which we wish to calculate.

To examine the natural convection during crystal growth, many simplifications are necessary. The simplifications will be enumerated and discussed briefly.

During crystal growth, a spontaneous change in the interface shape, known as morphological instability and convective instability will be coupled. Linear stability analysis [3] shows that the wavelength associated with the most unstable mode of convective instability is much larger than that associ-

ated with the most unstable morphological mode and, therefore, that the coupling between these instabilities is weak in specific parametric ranges. Because the linear coupling is weak and because we have little expectation at this stage that we can calculate the nonlinear coupling, we assume that the interface remains planar. The conditions for morphological stability in the absence of fluid flow are well known; we restrict the parameter range in our calculations to satisfy these conditions. In addition, we are neglecting deformation of the interface caused by the flow at present; the validity of this approximation can be estimated from the numerical results.

The convective flow field is assumed to be two-dimensional and periodic in the horizontal direction. The task of calculating the convective flow field is ultimately computational, and a two-dimensional computation is much more manageable than a three-dimensional one. The horizontal wavelengths for unstable convective modes calculated from linear stability analysis [1] are found to be much smaller than horizontal dimensions characteristic of experiments on unidirectional solidification except for very small growth velocities. Therefore, it is expected that the solutal convection above an interface will be periodic in the horizontal direction with a wavelength of the order of the most unstable mode determined from linear stability analysis. The model selected for computation is one horizontal cell of this periodic, cellular convection pattern: the length  $L$  in Figure 1a is taken to be one period.

The liquid is taken to be a Boussinesq fluid with constant properties (density  $\rho$ , kinematic viscosity  $\nu$ , liquid thermal diffusivity  $\kappa$ , solute diffusivity  $D$ , etc.) satisfying the Navier Stokes equations. In the Boussinesq approximation the density of the fluid is assumed to be constant everywhere except in the buoyancy terms where density variations are multiplied by the

acceleration of gravity  $g$ . This is a very common approximation which is excellent in the present application [2].

In order to compute the flow field, a finite region must be defined. As discussed above, one cell of a periodic convection pattern in the horizontal direction is selected. In the vertical direction, an artificial upper boundary is imposed. As noted earlier, the temperature gradient will tend to stabilize the convection. Therefore, the temperature field can be expected to limit the height of each convection cell, and if the artificial upper boundary is far enough from the interface, it should not influence the convection. (This assumption can be tested by changing the location of the artificial boundary.)

Between the liquid and the solid phase of the material, there will, in general, be a density change. This density change is usually small, and in this study we have neglected it.

### The Equations

A recent review of interfacial and hydrodynamic instability relevant to crystal growth has been given by Coriell and Sekerka [3]. The equations and boundary conditions governing double diffusive convection are presented as Eqs. (2) - (13) in that review. The equations are the Navier-Stokes equations for a buoyant fluid of constant properties in the Boussinesq approximation, conservation of energy in the liquid (a convection-diffusion equation for temperature), conservation of energy in the solid (a diffusion equation for the temperature in the solid) and conservation of solute (a diffusion-convection equation for the solute concentration). The equations are written in a reference frame which moves vertically upward at the constant interface

velocity. The equation of state for the fluid relates variations in the density from a reference state linearly to changes in temperature and in concentration.

The boundary conditions are obtained from conservation of mass, energy and solute concentration together with a no slip condition for the tangential component of velocity at the interface. Since we do not allow the interface to deform, we can not satisfy all of the usual solidification boundary conditions. In particular, we do not require that the interface temperature equal the equilibrium temperature. Linear stability calculations have indicated that this does not have a great effect on the conditions for the onset of convection. A simplified set of these equations, obtained by invoking the approximations enumerated above, are used to compute double diffusive convection in the present study.

When no convection occurs and the interface remains planar, a quiescent steady state exists in a reference frame moving with the constant interface velocity. This steady state is discussed in some detail, and mathematical expressions for the temperature and solute concentration fields are given in References 1 and 3. The fields are shown schematically in Figure 1.

For the computation, a set of dimensionless variables has been used. The dimensionless concentration is referenced to the equilibrium-state concentration  $C_{\infty}$  at infinity and the temperature gradients are made dimensionless using the equilibrium-state temperature gradient  $G_L$  in the liquid at the interface. All lengths are made dimensionless with respect to the height  $H$  of the enclosure used for computation and the time scale is based on the kinematic viscosity  $\nu$  of the fluid and the height of the enclosure.

When the equations are made dimensionless, several nondimensional parameters result:

$$\begin{aligned}
 Ra &= \frac{g\alpha G_L H^4}{\nu\kappa} \quad , \quad Ra_c = \frac{g\alpha_c C_\infty H^3}{\nu D} \\
 Pr &= \nu/\kappa \quad , \quad Pr_s = \nu/\kappa_s \\
 Sc &= \nu/D
 \end{aligned}
 \tag{1}$$

Here  $g$  is the acceleration of gravity.  $Ra$  is the Rayleigh number,  $\alpha$  being the coefficient of thermal expansion and  $Ra_c$  is the solutal Rayleigh number,  $\alpha_c$  being the coefficient of expansion for solute. The density in the liquid is given by the expression  $\rho = \tilde{\rho}_0 [1 - \alpha(T - \tilde{T}_0) - \alpha_c(C - \tilde{C}_0)]$  where  $\tilde{\rho}_0$ ,  $\tilde{T}_0$  and  $\tilde{C}_0$  are all reference quantities.  $Pr$  is the Prandtl number,  $Pr_s = Pr \kappa/\kappa_s$  and  $Sc$  the Schmidt number. Additional dimensionless parameters are the geometrical ratio  $R = H/L$ , representing the height to the width of the computational enclosure,  $U = \frac{VH}{\nu}$  representing the dimensionless interface velocity, and two additional parameters related to material properties; these are  $k$ , the partition coefficient (the ratio of the solute concentration in the solid to that in the liquid at the interface), and  $\hat{k}$ , the ratio of the thermal conductivity in the solid to that in the liquid.

In terms of dimensionless variables and parameters, the quiescent equilibrium solute concentration in the liquid and the temperature in the liquid and solid are

$$\begin{aligned}
 c_o(y) &= 1 + \frac{1-k}{1-(1-k)[1-\exp(-USc)]} [\exp(-yUSc) - \exp(-USc)] \\
 T_o(y) &= \frac{A}{G_L H} - \frac{1}{UPr} \exp(-yUPr) \\
 T_{so}(y) &= \frac{A}{G_L H} - \frac{1}{UPr} + \frac{1}{UPr_s} \frac{G_s}{G_L} [1 - \exp(-UPr_s y)]
 \end{aligned}
 \tag{2}$$

Here,  $A$  is a reference temperature and  $G_s/G_L$  is the ratio of the solid to liquid temperature gradients at the interface. (For more discussion of the dimensional parameters required to specify the problem or of the equilibrium, quiescent steady state, see References 1 and 3.) This solute concentration field and temperature field, together with a zero fluid velocity field, are the initial conditions for the convection computations described below.

The equations in dimensionless form which describe the double diffusive convection are

$$\frac{\partial \omega}{\partial t} - U \frac{\partial \omega}{\partial y} + \frac{\partial}{\partial x}(u\omega) + \frac{\partial}{\partial y}(v\omega) = \nabla^2 \omega + (Ra/Pr) \frac{\partial T}{\partial x} + (Ra_c/Sc) \frac{\partial c}{\partial x} \quad (3a)$$

$$\frac{\partial c}{\partial t} - U \frac{\partial c}{\partial y} + \frac{\partial}{\partial x}(uc) + \frac{\partial}{\partial y}(vc) = (1/Sc) \nabla^2 c \quad (3b)$$

$$\frac{\partial T}{\partial t} - U \frac{\partial T}{\partial y} + \frac{\partial}{\partial x}(uT) + \frac{\partial}{\partial y}(vT) + v \frac{dT_0}{dy} = (1/Pr) \nabla^2 T \quad (3c)$$

$$\nabla^2 \psi = -\omega \quad (3d)$$

$$u = \frac{\partial \psi}{\partial y}, \quad v = -\frac{\partial \psi}{\partial x} \quad (3e)$$

in  $0 \leq x \leq 1/R$ ,  $0 \leq y \leq 1$ , and

$$\frac{\partial T_s}{\partial t} - U \frac{\partial T_s}{\partial y} = (1/Pr_s) \nabla^2 T_s \quad (3f)$$

in  $0 \leq x \leq 1/R$ ,  $-1 \leq y \leq 0$ .

The boundary conditions are

at the top,  $y = 1$ ,

$$u = v = 0 \quad , \quad c = 1 \quad \text{and} \quad \frac{\partial T}{\partial y} = 0 \quad (4a)$$

at the bottom,  $y = -1$ ,

$$\frac{\partial T_S}{\partial y} = 0 \quad (4b)$$

at the sides,  $x = 0$  and  $x = 1/R$ , periodic boundary conditions:

$$\psi(x=0, y) = \psi(x=1/R, y)$$

$$\omega(x=0, y) = \omega(x=1/R, y)$$

$$c(x=0, y) = c(x=1/R, y)$$

$$\frac{\partial c}{\partial x}(x=0, y) = \frac{\partial c}{\partial x}(x=1/R, y)$$

$$T(x=0, y) = T(x=1/R, y)$$

(4c)

$$\frac{\partial T}{\partial x}(x=0, y) = \frac{\partial T}{\partial x}(x=1/R, y)$$

$$T_S(x=0, -y) = T_S(x=1/R, -y)$$

$$\frac{\partial T_S}{\partial x}(x=0, -y) = \frac{\partial T_S}{\partial x}(x=1/R, -y)$$

for all  $0 \leq y \leq 1$ . Finally, at the interface  $y = 0$ ,

$$u = v = 0$$

$$\frac{\partial c}{\partial y} = -USc(1-k)c$$

$$T = T_S \quad \text{and} \quad k \frac{\partial T_S}{\partial y} = \frac{\partial T}{\partial y} \quad (4d)$$

Here  $u$  and  $v$  are the horizontal and vertical components of the velocity vector in the laboratory (stationary) reference frame,  $\psi$  is the stream function, and  $\omega \equiv \frac{\partial v}{\partial x} - \frac{\partial u}{\partial y}$  is the vorticity.  $T$  and  $T_s$  are the variations of the temperatures

from the initial steady-state temperature fields given in Eq. (2) within the liquid and solid respectively.  $\nabla^2$  is the two-dimensional Laplacian, and all other symbols have been defined previously.

A feature of the double diffusive convection for a binary alloy which makes it particularly challenging is the range of the parameters required to describe it. Equations (1) and the discussion following them demonstrate that the process is determined by nine dimensionless parameters, even with all the simplifications in modeling the process discussed earlier. The range of these parameters which one can hope to investigate must be severely limited therefore; examination of Reference 1 confirms this observation.

A second feature which makes the calculations challenging is the size of some of these parameters. In a liquid metal the Prandtl number is very small, of the order  $10^{-2}$ : hence the conduction of heat occurs much more rapidly than does the diffusion of vorticity or of solute. In the limit when the Prandtl number vanishes the temperature variation from the equilibrium value would also vanish.

These observations can be used formally to simplify the temperature equations as follows. Note first that  $Pr_s$  and  $Pr$  are approximately the same size. Therefore let

$$\begin{aligned} T &= Pr T_1 + Pr^2 T_2 + \dots \\ T_s &= Pr T_{s_1} + Pr^2 T_{s_2} + \dots \end{aligned} \tag{5}$$

Simultaneously, change the time scale to reflect the faster time for thermal conduction:

$$\text{let } \tau = \frac{\kappa t}{H^2} = \frac{\kappa}{\nu} \frac{\nu t}{H^2} = \frac{1}{\text{Pr}} t \quad (6)$$

where  $t$  is the dimensional time. Now, formally substitute expansions (5) into the temperature equations in Eqs. (3), and change to the new time variable  $\tau$

in these equations. Note that  $\frac{dT_0}{dy} = \exp(-yU\text{Pr}) \cong 1$  for small  $\text{Pr}$ , provided  $U$  is not too large, and equate all terms independent of  $\text{Pr}$  to zero. The resulting approximate temperature equations are, for  $0 \leq x \leq 1/R$ ,

$$\frac{\partial T_1}{\partial \tau} - \nabla^2 T_1 = -v \quad \text{for } 0 \leq y \leq 1 \quad (7)$$

$$\frac{\partial T_{s1}}{\partial \tau} - \frac{\kappa_s}{\kappa} \nabla^2 T_{s1} = 0 \quad \text{for } -1 \leq y \leq 0$$

The corresponding boundary conditions on  $T_1$  and  $T_{s1}$  are:

$$\text{at } y = 1 \quad \frac{\partial T_1}{\partial y} = 0$$

$$\text{at } y = -1 \quad \frac{\partial T_{s1}}{\partial y} = 0$$

$$\text{at } x = 0 \text{ and } x = 1/R \quad (8)$$

$$T_1(x=0, y) = T_1(x=1/R, y)$$

$$\frac{\partial T_1}{\partial x}(x=0, y) = \frac{\partial T_1}{\partial x}(x=1/R, y)$$

and at the interface,  $y = 0$ ,

$$T_1 = T_{s1} \quad \text{and} \quad k \frac{\partial T_{s1}}{\partial y} = \frac{\partial T_1}{\partial y} .$$

This formal procedure takes advantage of the small Prandtl number, reducing the nonlinear convection-diffusion equation for the temperature variation from the initial state in the liquid to a linear diffusion equation as a first approximation. The solution for  $T_1$  is then coupled into the vorticity equation in Eqs. (3) by the substitution  $T = PrT_1$ .

### The Numerical Method

The equations presented above have been solved by finite difference methods. A rectangular grid is defined over one period in the horizontal direction and between the interface and the artificially imposed boundary at the top for the convection calculation. A similar grid is imposed over a horizontal period and between the interface and a second artificial boundary in the solid at  $y = -H$  to calculate the temperature in the solid. At the nodes or intersection of this grid all dependent variables are defined.

The equations solved numerically are the vorticity equation, (3a), the solute concentration equation, (3b), the stream function equation, (3d), and the two approximate temperature equations, (7), for the deviation of the temperature from the initial state. Note that the vorticity, concentration and temperature equations are all parabolic in character: they determine the time evolution of these dependent variables. The vorticity and concentration equations are coupled, nonlinear, convection-diffusion equations. The temperature equations are linear to the first approximation for small Prandtl number.

In contrast, the equation for the stream function is elliptic and linear. A very brief description of the numerical techniques used to solve these equations and the checks used to ascertain the validity of the numerical solutions will be presented.

For the two coupled nonlinear equations for concentration and vorticity, Fromm's method [4] was used. In this method, the convective terms, written in conservation form (as presented in Eqs. (3a) and (3b)), are approximated by central differences. The diffusion terms and the time derivatives are approximated according to the method of DuFort-Frankel [5]. Fromm's method is characterized as second order accurate in both space and time, explicit and a conservative scheme.

The solution to the coupled concentration and vorticity equations when the temperature field was suppressed (for example by setting  $Ra = 0$ ) was checked by solving these equations using a different finite difference scheme, the alternating direction implicit (ADI) scheme [6]. A typical mesh used for solution of the equations is 16 mesh cells in horizontal direction and 31 mesh cells in the vertical direction, and for such a mesh, the solutions obtained by the two different methods agreed to a few percent. The ADI scheme was found to take about three times longer to compute a transient solution, however, and therefore was not pursued.

The two linear temperature equations were also solved by two different methods, DuFort-Frankel and ADI, and agreement was found to a few percent. In this case, however, the ADI was found to be about a factor of ten times faster for small Prandtl number; the implicit nature of the scheme allowed time steps for the temperature computation of the same size as those for the vorticity computation without much accuracy degradation. Therefore, the ADI is presently being used to compute the temperature.

The elliptic equation for the stream function, given the vorticity field, was solved using a package developed by Swarztrauber and Sweet [7]. This package uses fast direct methods, fast Fourier transforms and cyclic reduc-

tion, and has been found in this and other applications to be both very accurate and efficient.

The algorithms for calculating the coupled concentration and vorticity equations are described in detail in Reference 8. They were implemented and checked by Mr. Winston Chuck during the summer of 1979 after he had graduated from Cornell University and before he entered a Ph.D. program at the University of Minnesota. The graphics display, using the NCAR graphics package [9], as shown in this report and initial attempts to compute the temperature field coupling to the vorticity and concentration distributions were carried out by Mrs. Kathleen Morrish during the summer of 1980, after she had completed her Masters degree at the University of Wisconsin and before she embarked on her Ph.D. at the University of Maryland. Her work is reported in Reference 10.

### Computational Results

Some computational results are given in Figures 2-7. Dimensionless parameters used in the computations are given in Table 1. The dimensional parameters used to obtain the values in Table 1 correspond to a cell height of .125 cm, a solutal diffusion coefficient of  $3. \times 10^{-5}$  cm<sup>2</sup>/s, an interface velocity of  $2. \times 10^{-3}$  cm/s, and temperature gradients of 500 K/cm and 200 K/cm for the first and second columns, respectively.

Figures 2 through 5 show contours of constant concentration and contours of the stream function at two different times. In the steady state, the stream function determines the flow magnitude and direction; the flow velocity is tangent to the stream function contour. The calculation is initiated by adding a small perturbation to the concentration profile and allowing the disturbance to develop from rest. In this case the bulk concentration is

25% larger than its critical value as predicted by linearized analysis [1]. In the early part of the calculation (Figures 2 and 3), a slight distortion of the concentration profile gradually appears. The cellular structure of the stream function contours shows good qualitative agreement with that of the linearized treatment. This initial period of slow growth is followed by a rapid, nonlinear growth over a relatively short time interval, leading to a steady state flow pattern with significant distortions of the concentration profile.

Figures 4 and 5 show the steady state pattern which persists after the transient period has ended. A large distortion of the concentration field is evident, with an accompanying upwelling of the streamlines near the center of the figure. Note also that the flow velocity remains orders of magnitude smaller near the upper boundary of the figure, demonstrating that the stabilizing temperature gradient has effectively "capped" the vertical extent of the flow. Therefore, the boundary conditions applied to the upper surface may not have too serious an influence on the flow.

Figures 6 and 7 correspond to a flow with larger Schmidt number,  $Sc = 10$ . In this case, a longer time is required to achieve a steady state, and the influence of the upper boundary determines the height of the convection cell. The vertical velocity near the center of the cell is  $1.0 \times 10^{-2}$  cm/s, which is about five times the speed of the interface. If the concentration far from the interface is normalized to unity, the maximum concentration at the interface is 3.72 and the minimum concentration is 2.23. The maximum and minimum temperatures along the interface differ by .013K.

For the two calculations shown above, it is valuable to check the static stability of the initial state; the fluid is statically stable if the density

decreases with height above the interface. For static stability  $\frac{d\rho_0}{dy} < 0$ , or in dimensionless form

$$\frac{Ra}{Pr} \frac{dT_0}{dy} + \frac{Ra_c}{Sc} \frac{dc_0}{dy} \geq 0$$

At the interface, where the concentration gradients are largest,

$$\frac{Ra}{Pr} - \frac{(1-k)USc}{1-(1-k)[1-\exp(-US_c)]} \frac{Ra_c}{Sc} \geq 0$$

Using the values given in Table 1, we find that the fluid is statically stable initially for both cases.

As an overall check on the computational scheme, the solutal Rayleigh number for convective instability was determined for prescribed values of all other parameters, and this value was compared with that determined by linear stability analysis as described in Reference 1. For a Rayleigh number of 0 and an aspect ratio of 0.5 and all other parameters as given in the first case shown in Table 1, the convection code was run repeatedly with increasing values of the solutal Rayleigh number until the initial, small perturbation either clearly decayed or grew. In the former case the flow was judged stable for that solutal Rayleigh number and in the latter case unstable. Linear stability analysis [1] determines the critical solutal Rayleigh number to be 4251. Using increments of 250 in  $Ra_c$  on a 16 by 31 mesh,  $Ra_c = 4500$  was determined to be stable whereas  $Ra_c = 4750$  was found to be unstable. The discrepancy between the critical solutal Rayleigh number determined from the convection code and that determined by linear stability analysis is between 6 and 12%. No attempt was made to determine the critical solutal Rayleigh using the convection code more precisely because near neutral stability, decay or growth of a perturbation was found to be very slow. Subsequent calculations with the convection

code have used estimates made by the linear stability analysis (with a nominal 10% variation) as a guide for selection of parameters.

The double-diffusive convection code described here offers the opportunity to examine nonlinear features produced by solutal convection during unidirectional solidification of a binary alloy. Although the range of parameters over which the code has been run is very limited at this time, we hope to extend this range in the future and to explore such nonlinear features as the magnitude of the convection and the distance above the interface to which convection extends as a function of Rayleigh number, solutal Rayleigh number and Schmidt number for example.

## EXPERIMENTAL

### Background

To grow from the melt a crystal containing a uniform concentration of a solute generally requires solidification at steady state with a planar solid-liquid interface. Convective instabilities of the liquid phase or morphological instabilities of the solid-liquid interface lead to a breakdown of these idealized solidification conditions, with resultant inhomogeneities of the crystal. In a previous article [11] we described a stability analysis of the succinonitrile-ethanol system which predicted the conditions of solute concentration and interface velocity which lead to convective or morphological instabilities. The analysis assumed an initially planar horizontal interface (unidirectional heat flow) of infinite extent. Succinonitrile was chosen as the primary constituent because it is a transparent material which solidifies with an unfaceted solid-liquid interface, which implies that deviations of the interface from its equilibrium temperature are negligible. The relevant physical properties of succinonitrile are well known. Ethanol is used as the solute because of its significantly lower density compared to succinonitrile. The relevant portions of the phase diagram have been reported previously. The liquidus slope for ethanol in succinonitrile is 3.6 K/wt.% and the solidus slope is 81 K/wt.%, giving a distribution coefficient of  $k = 0.044$ . Because of the low value of the distribution coefficient, the convective and interfacial instabilities of interest occur at low concentrations of ethanol, and very high purity starting materials are therefore required. Fortunately, it has already been demonstrated [12] that sufficient purity can be attained in succinonitrile by vacuum distillation and zone refining, and these methods have been used in the present experiments.

The stability analysis predicts that when succinonitrile containing ethanol solidifies unidirectionally upward, there exists for a given temperature gradient in the liquid a critical concentration above which plane-front convectionless solidification is unstable. This concentration is a function of the solidification velocity, and at low velocities the instability appears first in a convective mode whereas at higher velocities the instability appears first in an interfacial mode (Figure 8). The instability wavelength for the convective mode is considerably larger than that for the interfacial mode. For temperature gradients which are appropriate for Bridgman-type crystal growth in this system (about 10 K/cm) the transition from the convective to the interfacial instability mode occurs at velocities of a few micrometers per second. Moreover, there exists a range of concentrations between approximately  $2 \times 10^{-3}$  to  $5 \times 10^{-3}$  wt.% ethanol for which it is predicted that there is a range of solidification velocities in which plane front convectionless solidification is stable, but above which interfacial instabilities occur and below which convective instabilities occur. A sample was therefore prepared to be within this concentration range so that both types of instability could be sought.

#### Experimental Procedures

Samples of pure succinonitrile and succinonitrile doped with ethanol are sealed under vacuum in round pyrex tubes 19 mm in diameter. Composition is determined by measurement of the melting range, i.e., the difference between the liquidus temperature (where the last fragment of solid is equilibrated with the melt) and the solidus temperature (where liquid first appears at grain boundaries and in the form of droplets within the solid). The samples primarily used in these studies were determined thus to have melting ranges

of  $1.2 \times 10^{-2}$  °C, corresponding to  $1.5 \times 10^{-4}$  wt.% ethanol or equivalent (designated as the high purity sample), and 0.215 °C, corresponding to  $2.6 \times 10^{-3}$  wt.% ethanol. The samples are innocuated with microspheres of polyvinyltoluene to serve as markers for convective flow in the liquid.

Solidification is carried out by drawing the sample downward through a temperature gradient device consisting of a lower, low-temperature water jacket which is maintained below the melting temperature and an upper high temperature jacket which in some experiments consisted of a water jacket and in others consisted of an electric heater. A temperature gradient was thus established, typically in the range of 5-10 °C per centimeter.

The solid-liquid interface was observed and photographed through a stereomicroscope, directed horizontally at the region in which the temperature gradient was established. Bright field illumination was used for best observation of interface shapes but dark field illumination is most effective for observations of the particles which delineate the fluid flow. High resolution viewing of the material within the cylindrical tube requires that the tube be surrounded by a medium which is appropriately matched in refractive index to the tube contents. A mixture of water and ethylene glycol can be used for this purpose but more recently it has been found desirable to use a solid material as described below.

Succinonitrile is a somewhat unusual material in that the thermal conductivity of the solid and liquid are almost identical. Thus, when no solidification is taking place the gradients in the solid and liquid on either side of the interface are also identical. When the sample tube is held in a vertical temperature gradient, the linear gradients in the sample and in the container walls are thus matched and the isotherms, including that which coincides with

the solid-liquid interface, are almost planar and horizontal. When solidification is induced by drawing the sample downward, the emission of latent heat by the solid-liquid interface results in a discontinuity of temperature gradient across the interface, and because this discontinuity is not matched in the container walls and refractive index matching medium, the isotherms, especially that delineating the solid-liquid interface, become non-planar. The temperature gradient in the region near the interface thus has radial components. An inevitable consequence of this non-planar interface and the associated radial gradients is the presence of a thermally-induced convective flow in the liquid phase. This takes the form of an upward flow along the central axis of the sample tube and a downward flow along the walls. The presence of this thermally-induced flow is disruptive to the development of the steady state solute fields as assumed in the analysis of convective and interfacial instabilities, and therefore, seriously interferes with the comparison of theory with experiment. The effect is particularly severe in the case of materials such as succinonitrile which have a low thermal conductivity compared to that of any useful container.

One way to significantly reduce the radial gradients in the vicinity of the solid-liquid interface is to add an auxiliary heater surrounding the sample tube at the location of the solid-liquid interface. Such a heater, if properly adjusted, can establish a gradient change in the container walls and the index matching medium which approximates that in the solidifying material. Several designs for such heaters have been investigated, and the most effective found to this point has been a single loop of small-diameter resistance wire embedded in a cast block of transparent metallurgical epoxy which fits closely around the sample tube (Figure 9). The epoxy block holds the wire in position

and also serves as an approximate refractive index matching medium. During crystal growth the sample tube slides through the epoxy block and the small space between the block and the tube is filled with a fluid (ethylene glycol) which is held in place by surface tension and which serves both as a heat transfer medium and an optical matching medium. The most difficult aspect of using such a device is that it changes the vertical position of the solid-liquid interface as well as the radial gradient, so that both the position and power of the ring heater must be adjusted to give the flattest solid-liquid interface.

### Results

Without the use of a ring heater, it is found that convection is present during solidification of even pure samples of succinonitrile. Because of radial heat losses, some convection is present even when the growth velocity is zero.

Figure 10 is an example of a double-exposure photograph of the liquid above the solid-liquid interface showing the double images of several marker particles in the liquid, from which convective flow can be measured. The dense stream of particles results from the break-up of an agglomeration of particles and does not indicate a region of unusual flow conditions. Figure 11 shows flow velocities measured from this photograph (with the long line indicating the dense stream of particles). The crystallization velocity in these samples was zero, and when crystallization starts the fluid flow field remains similar in shape but the velocities increase. Thus, Figure 12 gives, as a function of growth velocity, an example of the upward flow velocity at the center of the tube 2 mm above the solid-liquid interface for a particular fixed set of crystallization conditions (temperature difference between hot and cold bath, configuration of refractive index matching medium, insulation,

etc.). The fluid flow in this case (pure material) is due entirely to the radial gradients resulting from lateral heat losses and from the flow of heat between the sample and the chamber walls. The velocities of flow are small enough that the motion of the particles is not easily seen when viewed in real time through the microscope, but are large enough to seriously disrupt the development of any steady state one-dimensional distribution of solute as assumed in the theoretical analysis. Therefore, it can be expected that the crystallization conditions used for this set of experiments will not lead to the onset of interfacial and convective instability at quite the same concentrations and velocities predicted by the theory.

In high purity succinonitrile, the radial gradients and fluid flow patterns result in a solid-liquid interface which is concave upward to an extent which increases with increasing crystallization velocity, but which has no microstructural features except for grooves where grain boundaries or sub-boundaries intersect the solid-liquid interface. Any marker particles which impinge upon the interface are pushed by it but tend to accumulate in grain boundary grooves or trijunctions where they may become trapped by the solid when they accumulate in sufficient numbers or the velocity becomes high enough.

In the sample containing  $2.6 \times 10^{-3}$  wt.% ethanol, the theory predicts interfacial instability at solidification velocities above about  $10 \mu\text{m}/\text{sec}$  and convective instability at velocities below about  $2.5 \mu\text{m}/\text{sec}$ , with stability predicted between these velocities. The experiments with this sample are complicated by the presence of a bowl-shaped interface and thermally induced convective flow similar to that seen in the pure sample. At steady state with a growth velocity of  $10 \mu\text{m}/\text{s}$  it is found that this sample solidifies with a cellular solid/liquid interface, i.e., interfacial instability has

occurred. At a growth velocity of 6  $\mu\text{m}/\text{sec}$  it was found that approximately one half of the solid-liquid interface, in the central part of the sample tube, was in the form of a cellular interface while the outer part of the sample was non-cellular. At 4  $\mu\text{m}/\text{sec}$ , one fourth or less of the interface was cellular and at slower velocities no cellular structure was observed. Figure 13 contrasts the smooth but bowl-shaped interface of a high purity sample with a cellular interface in an ethanol-doped sample. Thus, the onset of interfacial instability occurred at or somewhat below the velocity at which it was predicted. At low velocities, where the convective instability is predicted, no flow patterns clearly distinguishable from those of the pure material could be distinguished among the background of purely thermal convection.

The localization of interfacial instabilities in the central portion of the sample tube was found to be a result of macroscopic shape change of the interface. These shape changes are consistent with what would be expected from the observed thermal convective flow patterns. Whereas the radial heat flow and associated thermal convection produce a bowl-shaped (i.e., concave upward) solid-liquid interface in both the pure and the ethanol-doped sample, in the latter sample the interface developed an additional central depression in the center which grew to a depth comparable to its width and then broke down into a classical cellular structure (Figure 14). No such central depression was ever seen in the pure material.

The development of the central depression in the interface only in the sample doped with ethanol suggests that it may be attributed to the accumulation of solute ahead of the interface directly under the point where the thermally-induced convective flow converges and turns upward.

In the sample containing  $2.6 \times 10^{-3}$  wt.% ethanol, the solidus and liquidus temperatures differed by 0.2 K. Interface temperature variations due to the lateral distribution of solute caused by the thermal convection can be expected to fall within this range. In a sample solidifying at  $2 \mu\text{m/s}$  in a temperature gradient of about 6 K/cm, it was found that the axial depression achieved a maximum depth of about 0.5 mm before the cellular structure developed. Thus, the interface temperature would vary by 0.3 K in a depression of this depth if we neglect the influence of the latent heat, in fair agreement with the melting point range.

When the same experiment was repeated but with the ring heater surrounding the interface activated to a power of 0.6 watts, the solid-liquid interface was greatly flattened and the central depression did not develop even after three hours of growth. As a result, the cellular interface did not develop. Although convection measurements were not made in this experiment due to particle viewing difficulties through the ring heater holder, the flatter shape of the interface clearly indicated a lower driving force for thermal convection.

### Conclusions and Discussion

The onset of convective and interfacial instabilities during the unidirectional upward solidification of succinonitrile containing ethanol has been predicted as a function of solute concentration and solidification velocity. At some concentrations it is predicted that there is a range of growth velocities in which solidification is stable, with interfacial instability predicted above this range and convective instability predicted below this range.

Experimental measurements of solidification in samples of succinonitrile solidified upward in a temperature gradient have shown that convection is present even in high purity samples, where it must be attributed to radial thermal gradients. The pattern of thermally-induced convective flow is consistent with the observed distortion of the solid-liquid interface due to heat exchange between the solidifying sample and the container walls. The thermally-induced convection interferes with any direct observation of the transition from stability to convective instability because solidification is not unidirectional as assumed.

Interfacial instability is never observed in a high purity sample, as predicted, and in a sample doped with  $2.6 \times 10^{-3}$  wt.% ethanol interfacial instability is found in the form of a cellular solidification front extending over the entire interface at velocities very close to that which is predicted. However, at slower growth velocities the cellular solidification front is also seen but covers only a restricted area at the center of the interface and at still slower velocities no cellular structure is seen.

The localization of the cellular structure in the central part of the interface was found to be the result of a macroscopic but transient depression which develops in that part of the interface. This depression, which is never seen in high purity samples, is attributed to solute redistribution by the thermally-induced convective flow. Activation of a ring heater surrounding the solid-liquid interface results in a flattening of the interface and thus a reduction in the driving force for thermal convection. Under these conditions, the formation of the central depression and of the cellular interface is suppressed.

Table 1. Values Used in Numerical Calculations

	<u>Figures 2 - 5</u>	<u>Figures 6 - 7</u>
$Ra_c$	55,000.	11,000.
$Ra$	152,900.	611.4
$Sc$	1.0	10.0
$Pr$	.01	.01
$Pr_s$	.01	.01
$U$	8.33	.833
$R$	1.10	.856
$k$	.3	.3
$\hat{k}$	1.0	1.0

## References

1. S.R. Coriell, M.R. Cordes, W.J. Boettinger and R.F. Sekerka, Convective and Interfacial Instabilities During Unidirectional Solidification of a Binary Alloy, *J. Crystal Growth* 49, 13 (1980).
2. J.S. Turner, *Buoyancy Effects in Fluids*, Cambridge University Press, London (1973), Chapter 8.
3. S.R. Coriell and R.F. Sekerka, Effect of Convective Flow on Morphological Stability, *PhysicoChemical Hydrodynamics* 2, 281 (1981).
4. J. Fromm, The Time Dependent Flow of an Incompressible Viscous Fluid, *Methods of Computational Physics*, Vol. 3, Fundamental Methods in Hydrodynamics, B. Alder, S. Fernbach and M. Rotenberg (eds), Academic Press, New York, (1964), pp. 345-382.
5. E.C. DuFort and S.P. Frankel, *Math. Tables and Other Aids to Computation*, 3, 135 (1953).
6. R.E. Richtmyer and K.W. Morton, *Difference Methods for Initial Value Problems*, Interscience Publishers, New York (1967), pp. 211-216.
7. P. Swarztrauber and R. Sweet, Efficient FORTRAN Subprograms for the Solution of Elliptic Partial Differential Equations, NCAR Technical Note 1A-1 (July 1975).
8. W. Chuck, A Model of Solutal Convection, Unpublished NBS Report, September 1979.
9. NCAR Graphics Software, edited by T. Wright, NCAR Technical Note (preliminary edition), April 1977.
10. K.A. Morrish, A Model of Double-Diffusive Convection, Unpublished NBS Report, August 1980.

11. R. J. Schaefer and S. R. Coriell, Convective and Interfacial Instabilities During Solidification of Succinonitrile Containing Ethanol, Materials Processing in the Reduced Gravity Environment of Space, ed. by Guy E. Rindone (Elsevier, 1982) p. 479.
12. R. J. Schaefer, M. E. Glicksman, and J. D. Ayers, High-Confidence Measurement of Solid/Liquid Surface Energy in a Pure Material, Phil. Mag. 32, 725 (1975).

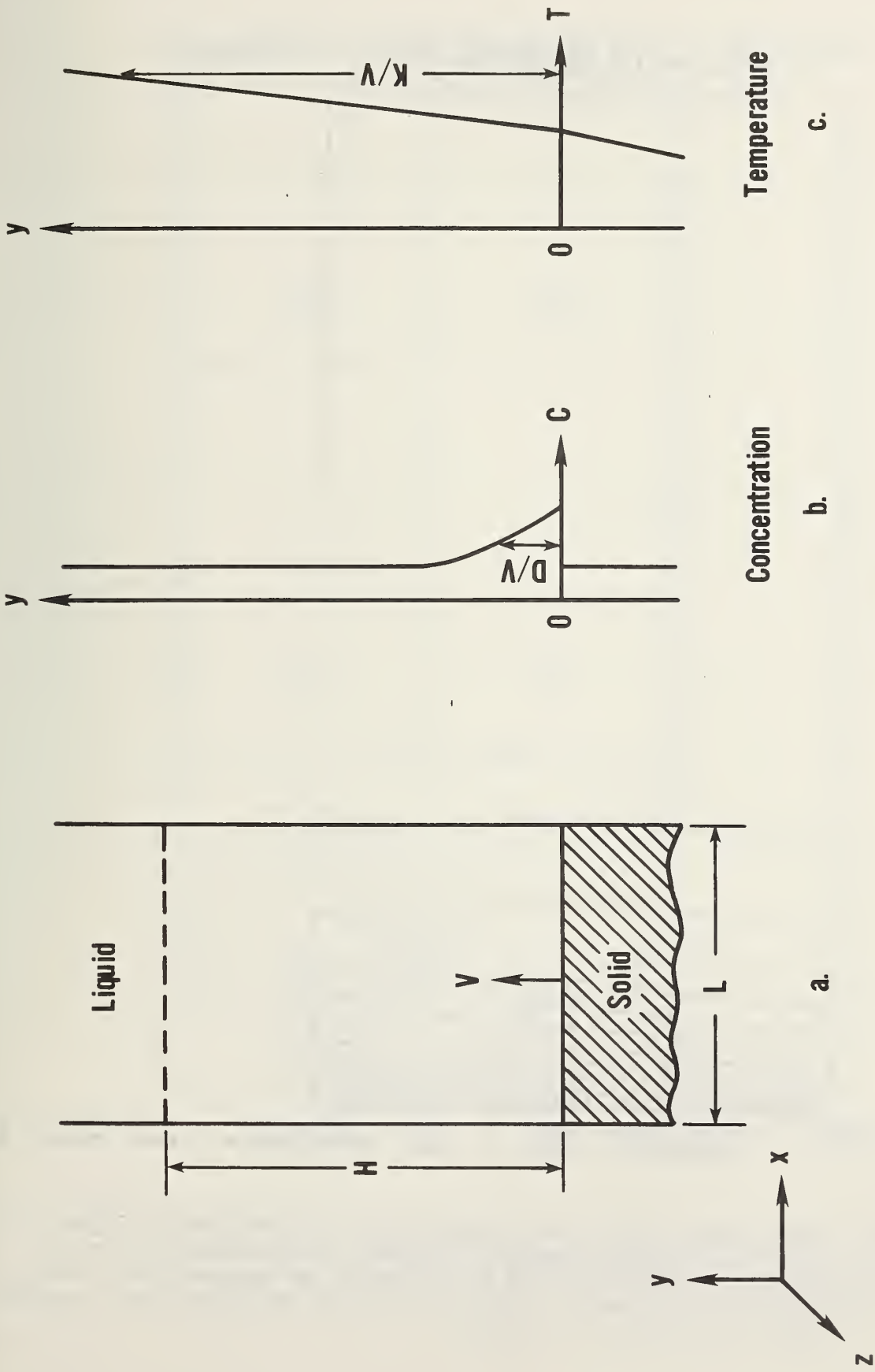
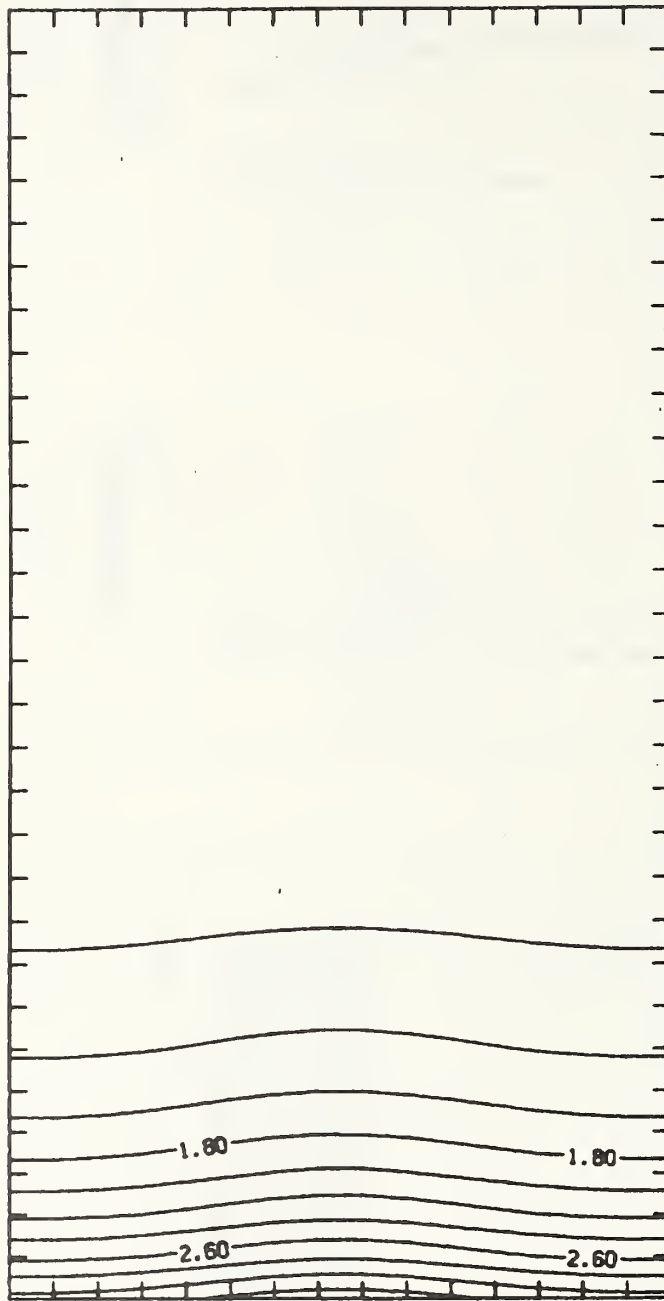


Figure 1.

Fig. 1. Schematic diagram of the initial state of the alloy.

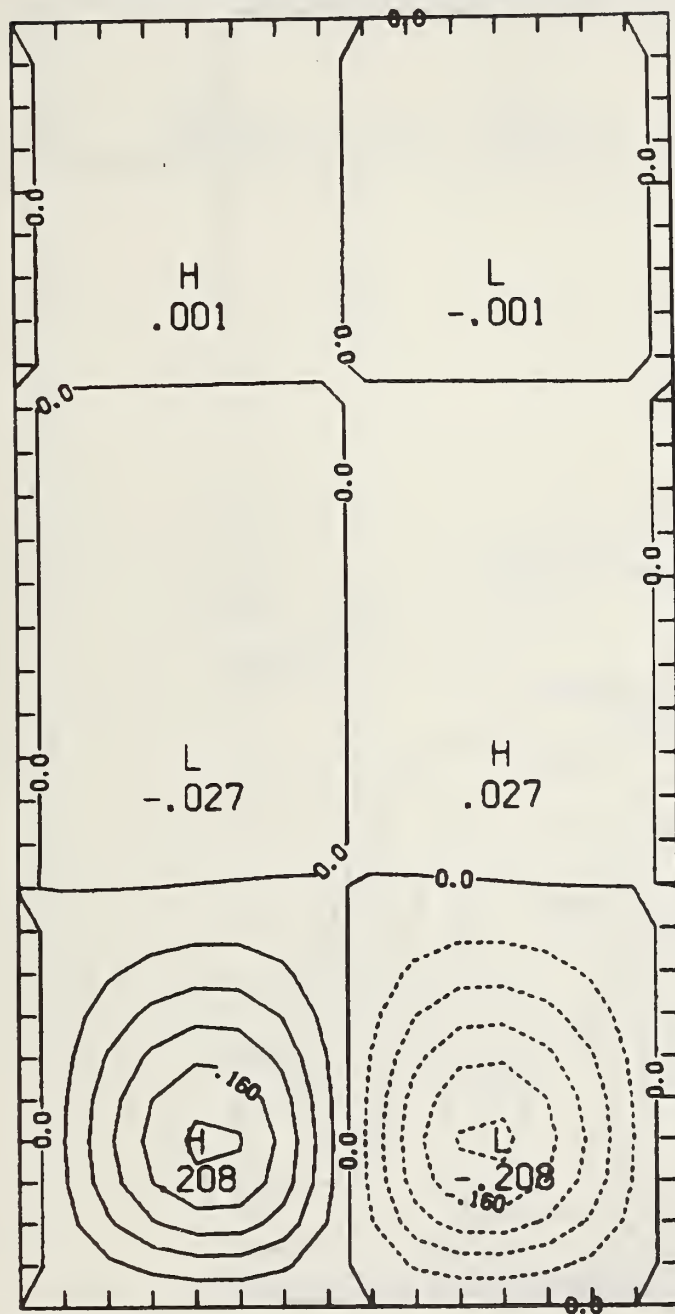
CONCENTRATION CONTOUR MAP AT T = 2.49749-01



CONTOUR FROM .80000 TO 3.2000 CONTOUR INTERVAL OF .20000 PT(19,3)= 2.1800

Fig. 2. Level lines of the concentration field at dimensionless time  $t = .25$ . The dimensionless parameters for this case appear in Table 1. The increment in the value of the concentration from one line to the next is constant, so that the lines bunch together where the gradients are large.

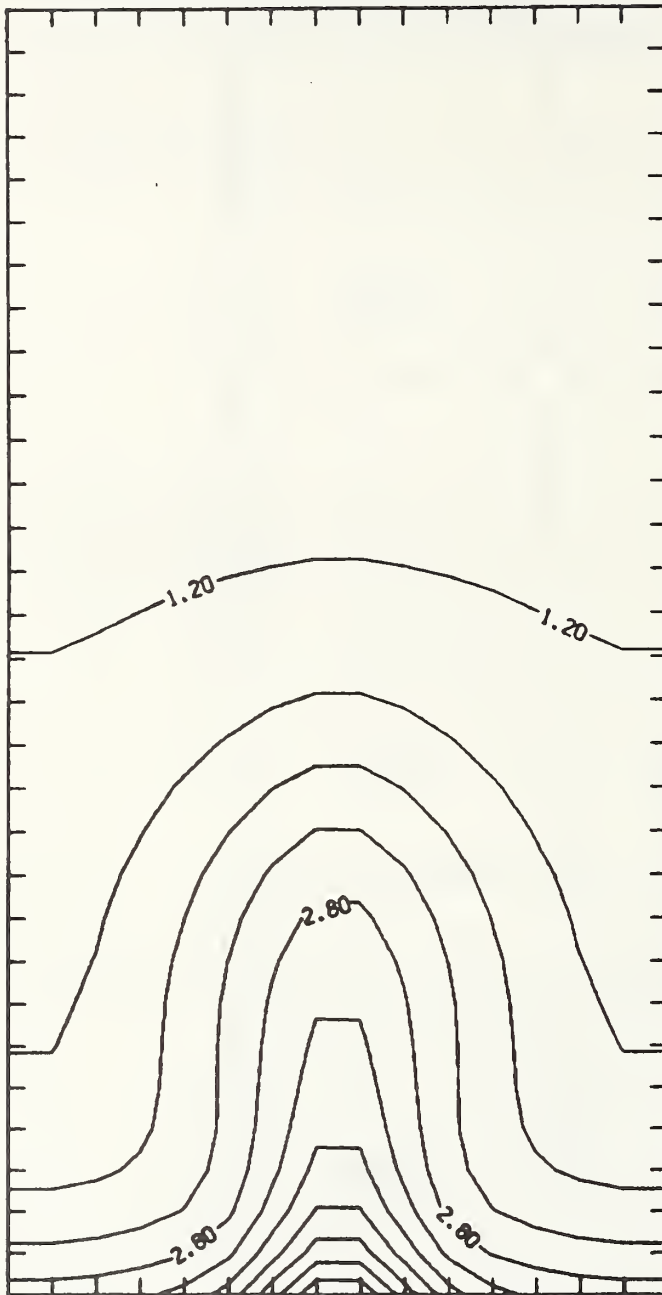
STREAM FUNCTION CONTOUR MAP AT T = 2.49749-01



CONTOUR FROM -.20000 TO .20000 CONTOUR INTERVAL OF .40000-01 PT(9.31) = .74143-01

Fig. 3. Level lines of the stream function at time  $t = .25$ . The instantaneous velocity is tangent to the level lines. The location and magnitude of the stream function's highs and lows are indicated in the figure.

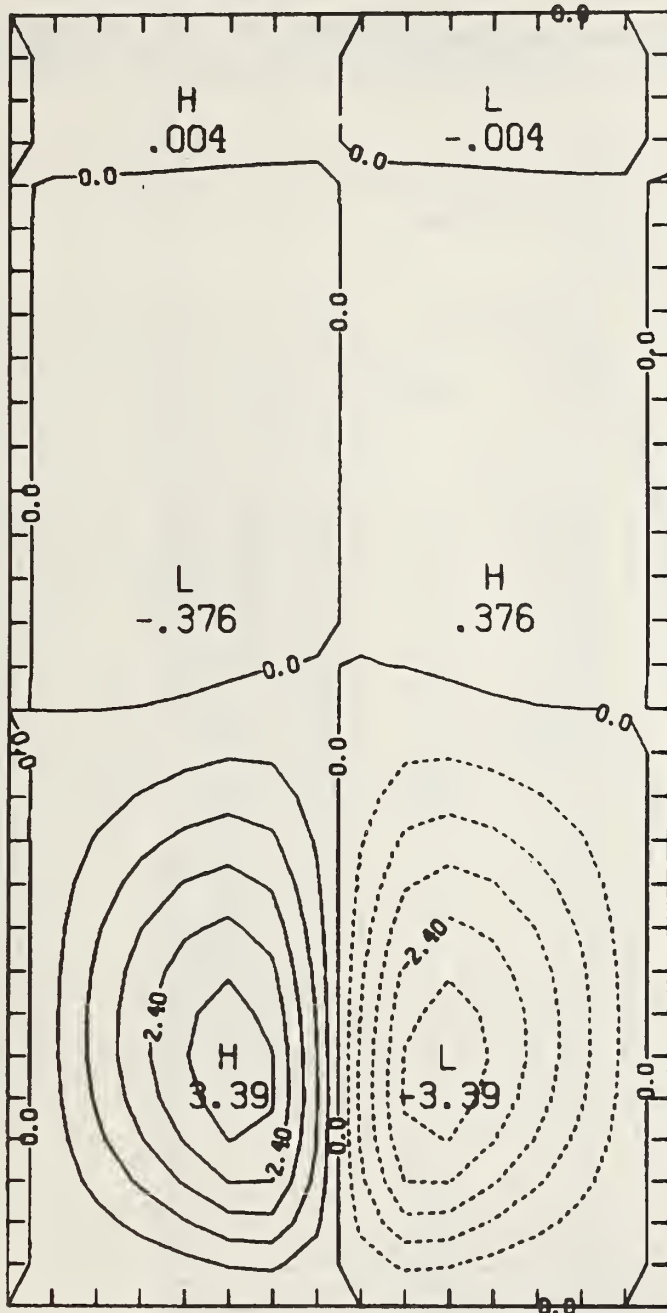
CONCENTRATION CONTOUR MAP AT T = 1.24974+00



CONTOUR FROM .80000 TO 5.2000 CONTOUR INTERVAL OF .40000 PT(3,9)= 2.1722

Fig. 4. Level lines of the concentration field at steady state.

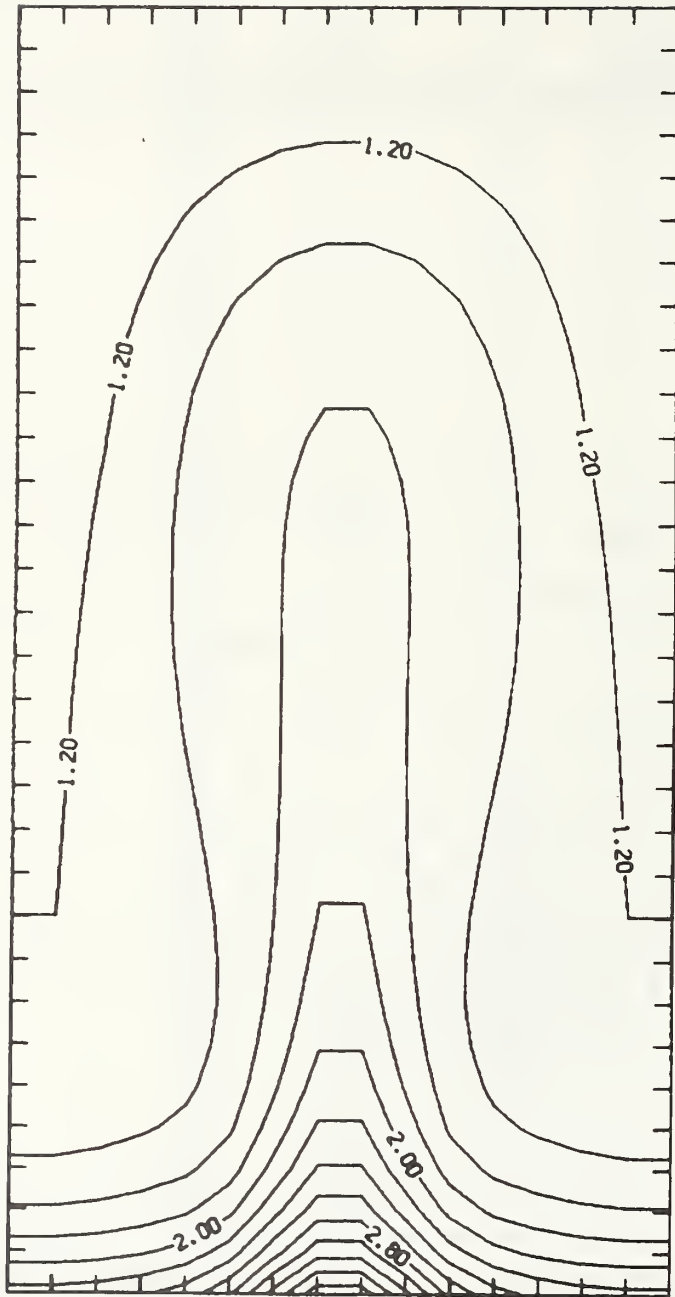
STREAM FUNCTION CONTOUR MAP AT  $T = 1.24974+00$



CONTOUR FROM -3.0000 TO 3.0000 CONTOUR INTERVAL OF .80000 PT(3,31) = .49845

Fig. 5. Level lines of the stream function at steady state.

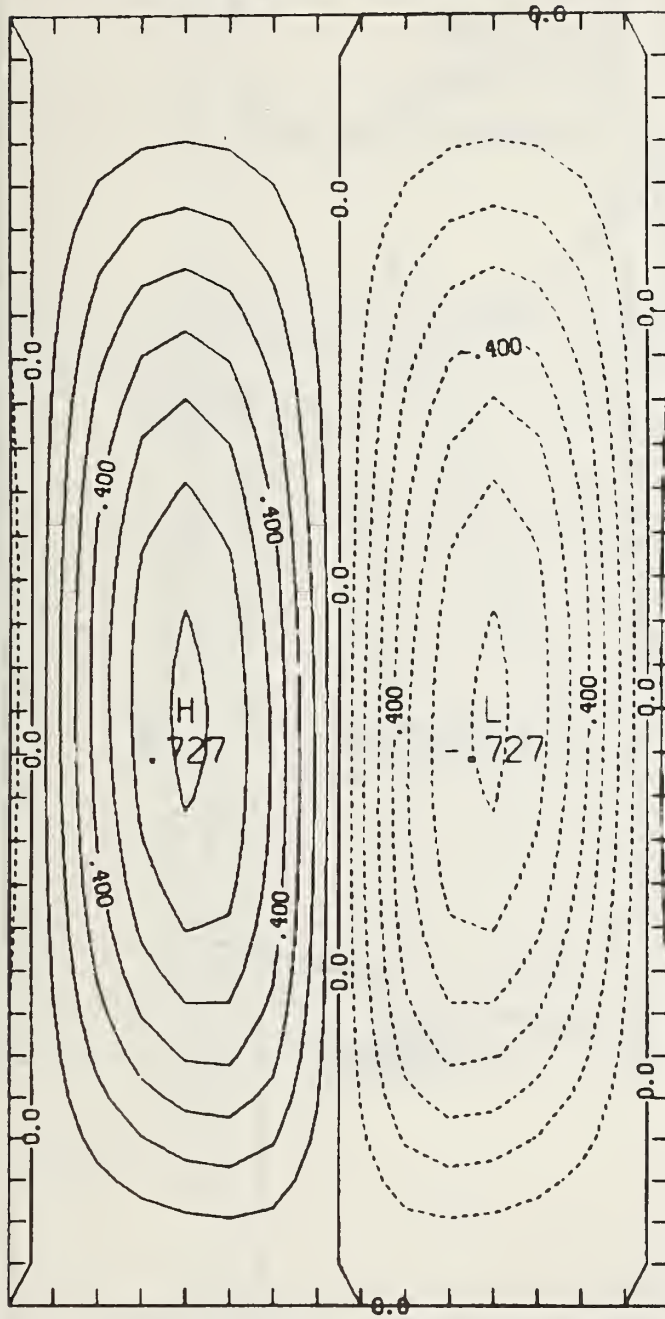
CONCENTRATION CONTOUR MAP AT T = 2.50019+00



CONTOUR FROM .80000 TO 3.6000 CONTOUR INTERVAL OF .20000 PT(3,9)= 1.6395

Fig. 6. Level lines of the concentration field at dimensionless time  $t = 2.5$ . The dimensionless parameters for this case appear in Table 1.

STREAM FUNCTION CONTOUR MAP AT T = 2.50019+00



CONTOUR FROM -.70000 TO .70000 CONTOUR INTERVAL OF .10000-00 PT(3.3)= .41280-01

Fig. 7. Level lines of the stream function at time  $t = 2.5$ .

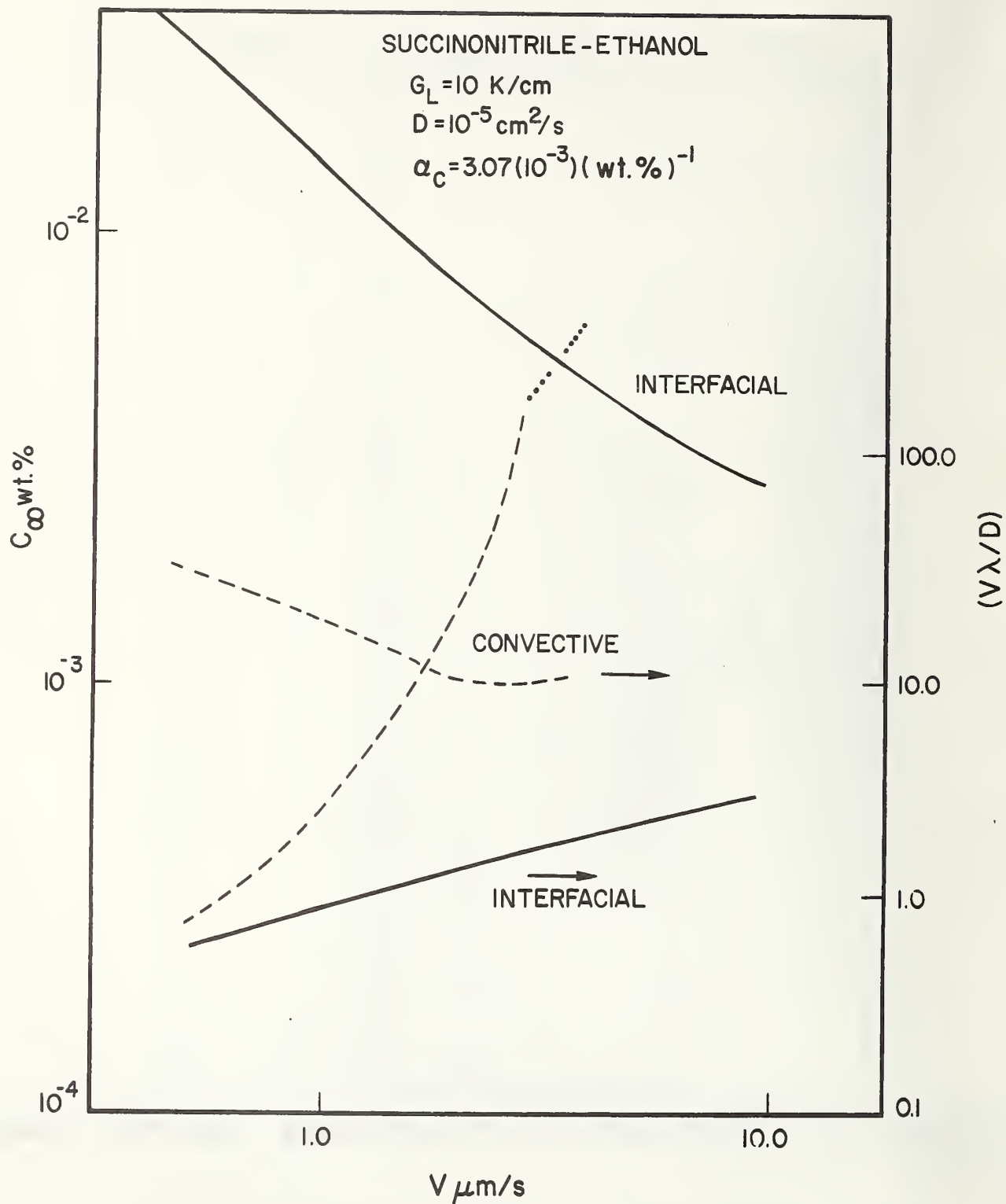


Fig. 8. The critical concentration  $c_\infty$  of ethanol in succinonitrile above which instability occurs as a function of the velocity  $V$  of unidirectional upward solidification for a temperature gradient in the liquid of 10 K/cm. The ratio of the instability wavelength,  $\lambda$ , to the diffusion boundary layer thickness,  $D/V$ , is also shown. The solid and dashed lines correspond to interfacial and convective instabilities, respectively, while the dotted line denotes an oscillatory convective instability.

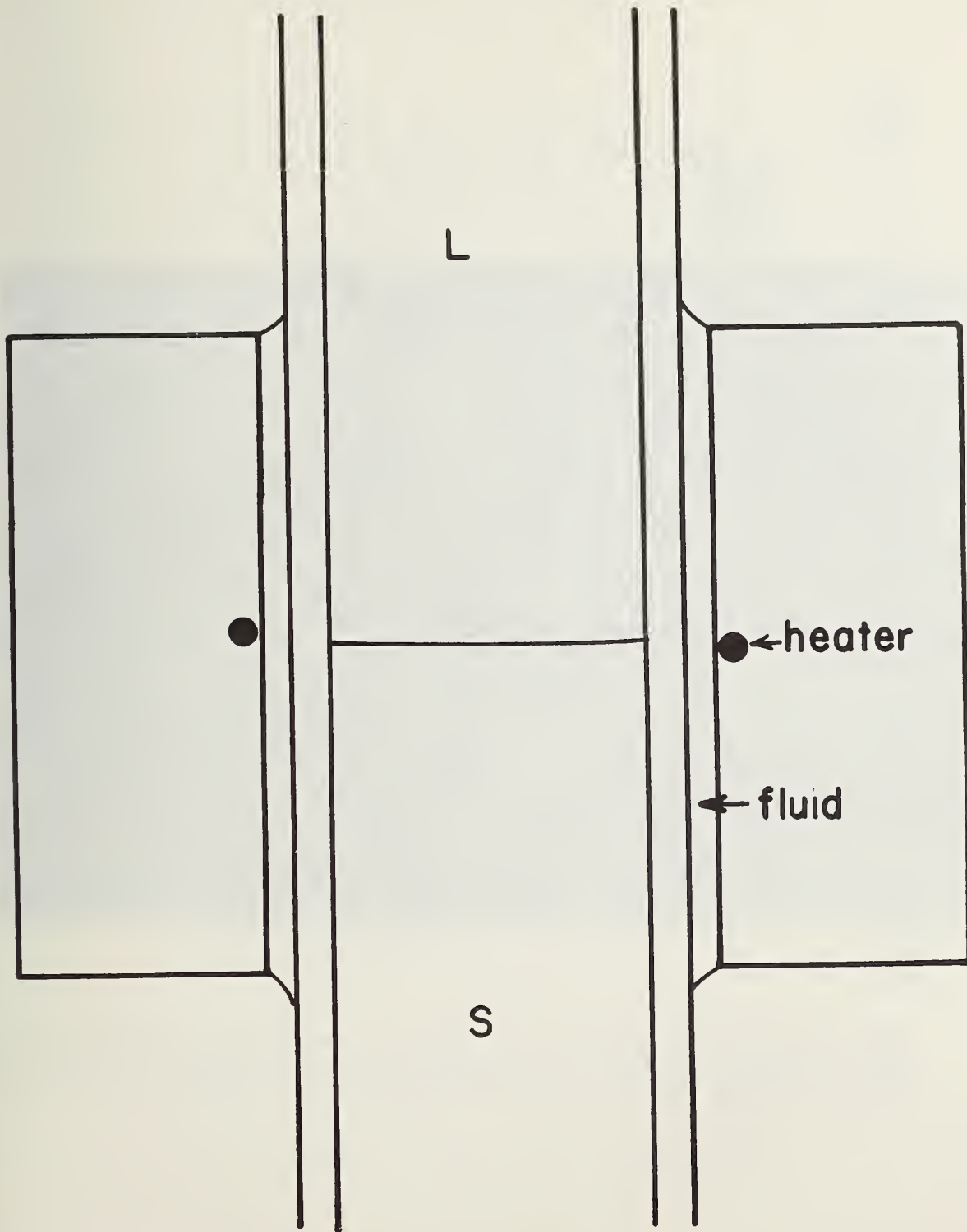


Fig. 9. Position of ring-shaped heater wire, embedded in transparent epoxy block surrounding the solid-liquid interface. A fluid layer between the epoxy block and the borosilicate glass sample tube is held in place by surface tension.



Fig. 10. Double-exposure photograph of 2  $\mu\text{m}$  diameter particles suspended in a sample of pure succinonitrile, showing motion in the liquid directly above the solid-liquid interface near the center of the sample tube.

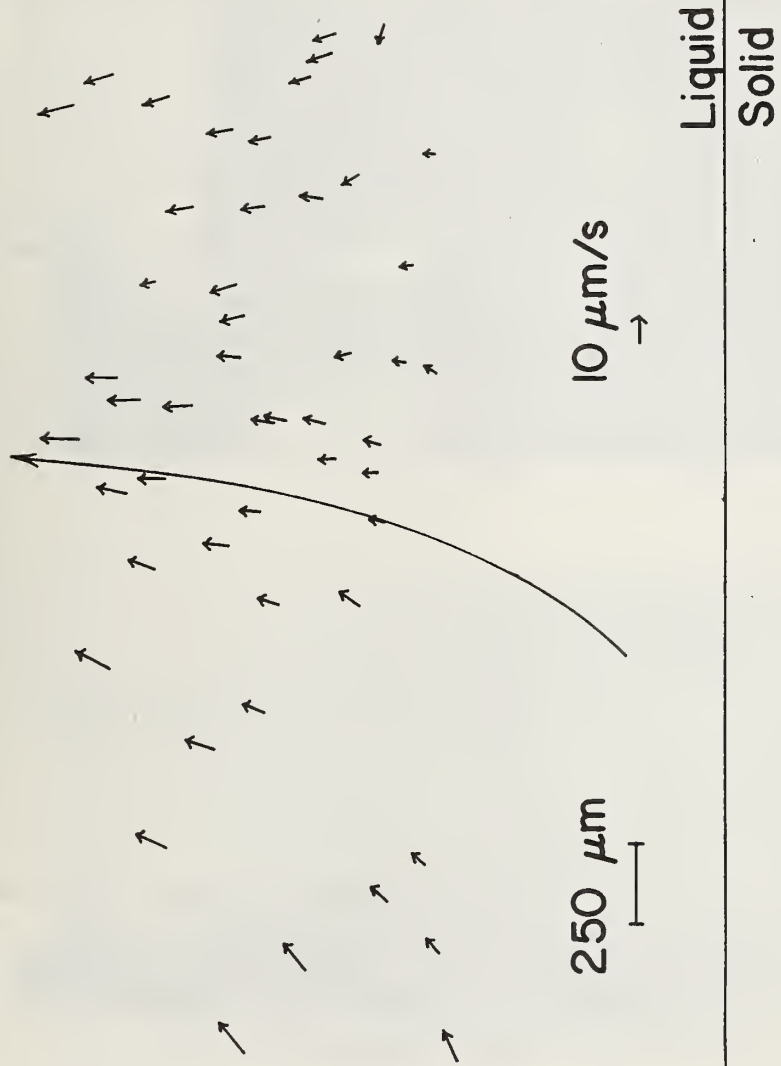


Fig. 11. Measured flow velocities from Figure 9, with the long arrow indicating the position of a concentrated stream of particles. The total inside diameter of the sample tube is  $17\ \text{mm}$ ; this diagram shows the central 20% of the tube diameter.

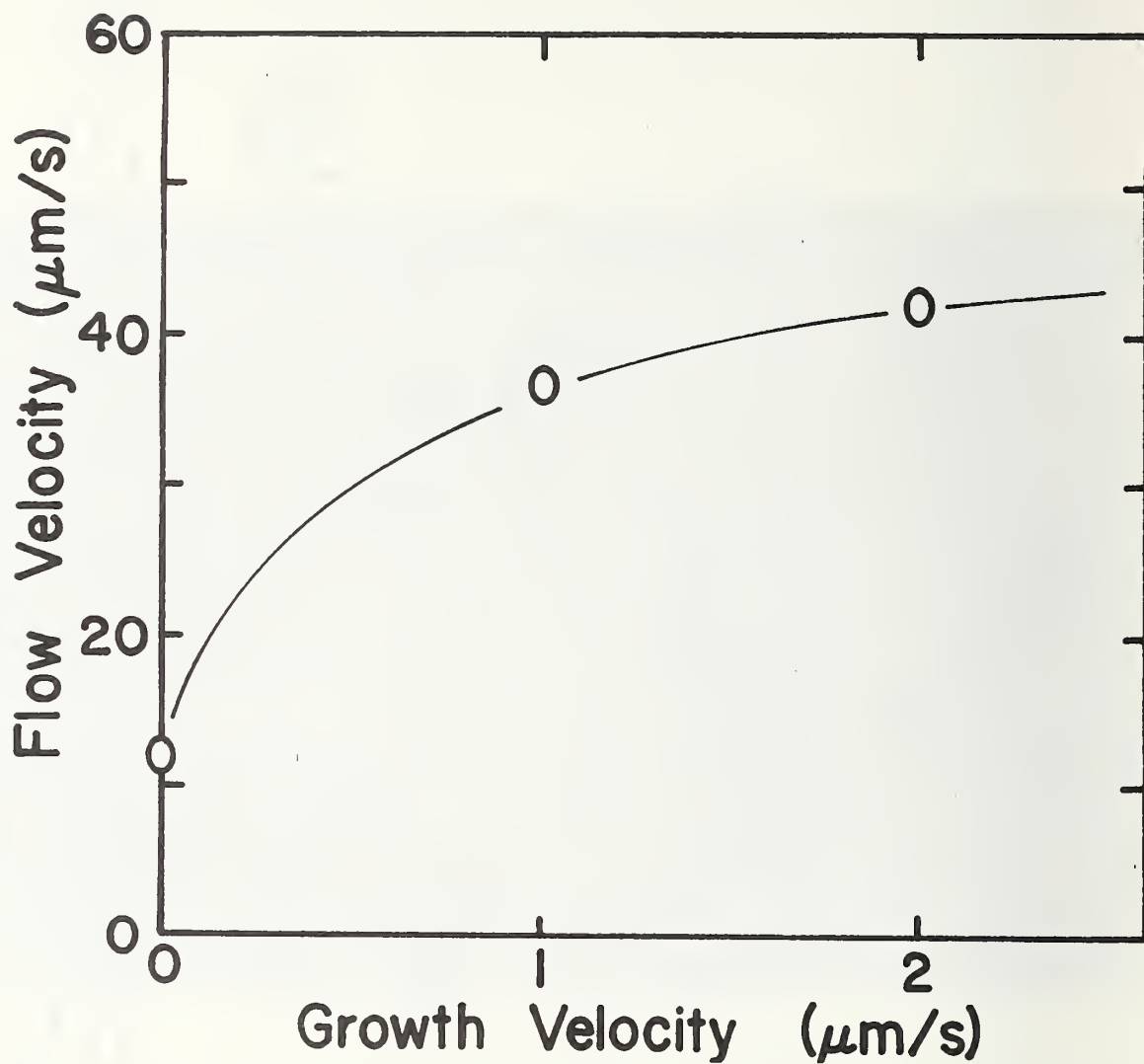


Fig. 12. Upward fluid flow velocity 2 mm above the center of the solid-liquid interface during solidification of the pure succinonitrile sample. This flow is purely thermal in origin and is due to both heat losses to the environment and (for non-zero growth velocities) to heat exchanges with the container walls in the vicinity of the solid-liquid interface.



Fig. 13. Smooth but bowl-shaped interface as seen during solidification of high-purity succinonitrile, contrasted to cellular interface seen at sufficiently rapid solidification velocities in ethanol-doped succinonitrile.



Fig. 14. The macroscopic depression which develops in the center of the solid-liquid interface of the ethanol-doped sample. Above, it is seen just at the point where interfacial instability has appeared, and below, it is seen after a cellular structure has developed.

MORPHOLOGICAL AND CONVECTIVE INSTABILITIES DURING SOLIDIFICATION

S. R. Coriell\*, R. F. Boisvert,\*\* J. I. Mickalonis\*\*\*, and  
M. E. Glicksman\*\*\*

\*Metallurgy Division, \*\*Scientific Computing Division  
National Bureau of Standards, Washington, D.C. 20234 USA

\*\*\*Materials Engineering Department  
Rensselaer Polytechnic Institute, Troy, N.Y. 12181 USA

ABSTRACT

The stability of the flow between two vertical, infinite, rigid, coaxial cylinders held at different temperatures is analyzed by linear stability theory. For a Prandtl number of 22.8 and a radius ratio of 0.02, the flow is unstable to an axisymmetric perturbation at a critical Grashof number of 2150; the wave speed of the instability is comparable to the maximum velocity of the unperturbed flow. When the rigid outer cylinder-fluid interface is replaced by a crystal-melt interface which can change shape, two new modes of instability occur at lower Grashof numbers. There is an asymmetric instability with a critical Grashof number of 180 and an axisymmetric instability with a critical Grashof number of 460; for both of these modes the wave speed of the instability is several orders of magnitude smaller than the unperturbed flow velocity.

These calculations were motivated by and are in general agreement with our recent experiments on succinonitrile. A long vertical cylindrical sample of succinonitrile was heated by an electrical current through a coaxial vertical wire so that a vertical melt annulus formed between the coaxial heater and the surrounding crystal-melt interface. Above a critical Grashof number of circa 200, a helical crystal-melt interface formed which rotated steadily about the cylinder axis; the wave speed was several orders of magnitude less than the base flow velocity.

## INTRODUCTION

There has been extensive research and development on the effect of fluid flow on solidification and on the properties of the resulting solid [1-3]. Both hydrodynamic instabilities [4] and morphological instabilities [5] have been studied and the effect of convective flow on morphological stability has been recently reviewed [6]. Delves [7] showed theoretically that a flow parallel to the crystal-melt interface could increase stability and give rise to traveling waves on the interface. The interaction of morphological instability with a melt subject to thermosolutal instability and the effect of gravity on this interaction has also been studied [8-9]. In both these cases, morphological instability occurs even in the absence of fluid flow, although in general the critical value of the parameter for the onset of instability is changed by the flow.

As illustrated in Figure 1, recent experiments [10-11] have demonstrated an interface instability under conditions for which in the absence of flow, the solid-melt interface would be morphologically stable. In these experiments, a long vertical cylindrical sample of high purity succinonitrile was heated by an electrical current through a long, coaxial, vertical wire, so that a vertical melt annulus formed between the coaxial heater and the surrounding solid-melt interface. The outer radius of the crystal was maintained at a constant temperature below the melting point ( $58.1^{\circ}\text{C}$ ). With this arrangement the temperature increases in the liquid and decreases in the solid with distance from the crystal-melt interface, and consequently the interface would be morphologically stable in the absence of fluid flow [6].

Buoyancy dictates that the fluid flows upward near the heated wire and downward near the crystal-melt interface. There are analytic solutions of the fluid flow and temperature equations in which the flow velocity is vertical and the flow velocity and temperature are functions of the radial coordinate alone. The instability of a similar flow between two infinite vertical plates has been reviewed by Gershuni and Zhukhovitskii [12]. Recently, Choi and Korpella [13] and Shaaban and Ozisik [14] used linear stability analysis to calculate the critical Grashof number for axisymmetric instabilities of the axisymmetric

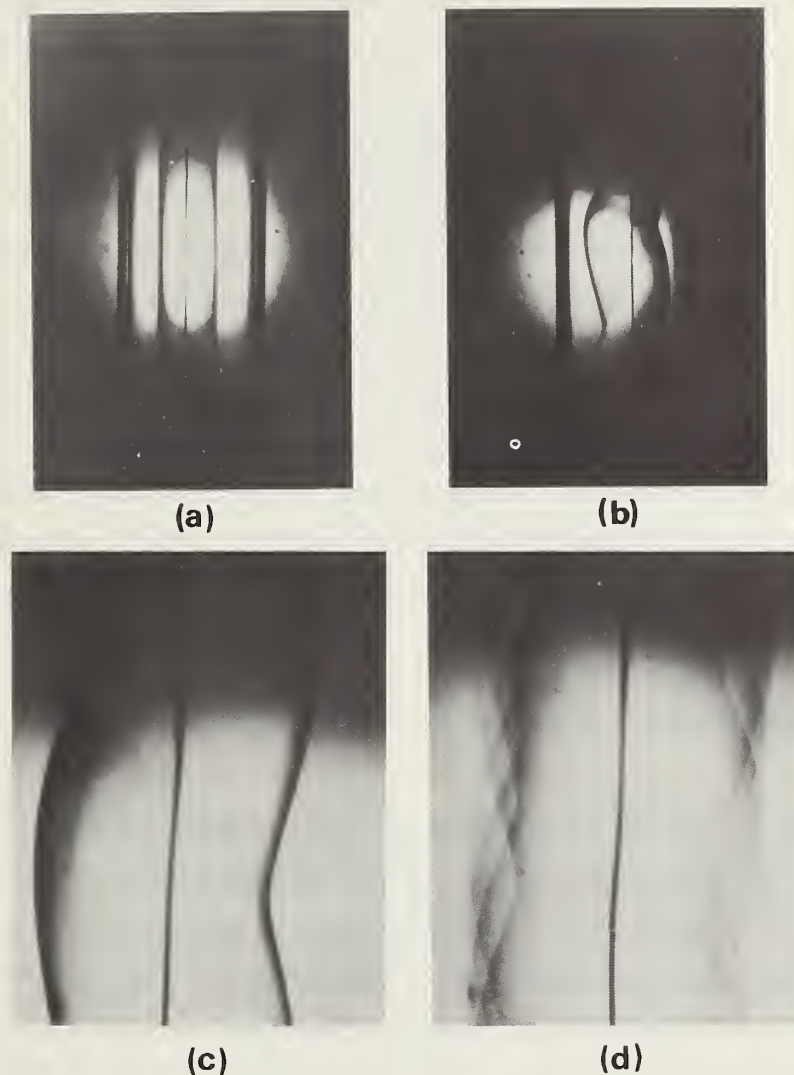


Fig. 1. A long vertical cylindrical sample of succinonitrile is heated by an electrical current through a coaxial vertical wire so that a vertical melt annulus forms between the wire and the surrounding crystal-melt interface. a) below a critical Grashof number of circa 200, the crystal-melt interface is cylindrical; b-d), above the critical Grashof number, a helical crystal-melt interface forms; d) multiple exposures show motion of the helical interface.

flow described above occurring between two vertical, infinite, coaxial cylinders held at different temperatures. We have analyzed this instability problem by a numerical technique different from that of references 13-14 for parameters more appropriate to the experiments described in references 10 and 11. In this case, the flow between two vertical infinite coaxial cylinders is unstable

to an axisymmetric perturbation above a Grashof number of 2150 and the wave speed of this perturbation is comparable to the unperturbed flow velocity.

In contrast, as illustrated in Figure 1 the experimental observations [10-11] with a crystal-melt interface indicate an asymmetric instability at a critical Grashof number of about 200 with a wave speed orders of magnitude less than the unperturbed flow velocity. Therefore, we have investigated the effect of a crystal-melt interface, which can change shape, on the stability of the flow between an infinite vertical cylinder maintained at a constant temperature and a coaxial crystal-melt interface. As will be described, the presence of the crystal-melt interface leads to additional modes of instability. The lowest mode is asymmetric with a critical Grashof number less than 200 and with a critical wave speed two orders of magnitude less than the unperturbed flow.

## THEORY

As illustrated in Figure 2 we consider a cylindrical coordinate system  $(\bar{r}, \bar{\phi}, \bar{z})$  such that the melt is contained in the infinite annular region  $\bar{r}_i \leq \bar{r} \leq \bar{r}_{sL}$  and the crystal is contained in the infinite annular region  $\bar{r}_{sL} \leq \bar{r} \leq \bar{r}_{sL} + \bar{L}_s$ , where  $\bar{r}_i$  is the radius of the inner cylinder (wire),  $\bar{r}_{sL}$  is the radius of the unperturbed solid-liquid-interface, and  $(\bar{r}_{sL} + \bar{L}_s)$  is the outer radius of the crystal. We define  $\bar{L} = \bar{r}_{sL} - \bar{r}_i$ ,  $\kappa = \bar{r}_i/\bar{r}_{sL}$ ,  $L_s = \bar{L}_s/\bar{L}$  and a dimensionless coordinate system  $(r, \phi, z) = (\bar{r}/\bar{L}, \bar{\phi}, \bar{z}/\bar{L})$ . Further we measure temperature in units of  $\Delta T$ , the difference between the temperature at  $\bar{r} = \bar{r}_i$  and the temperature of the unperturbed solid-liquid interface, time in units of  $\bar{L}^2/\nu$ , and the fluid flow velocity in units of  $g\alpha\bar{L}^2\Delta T/\nu$ , where  $g$  is the acceleration of gravity, which is in the negative  $z$ -direction,  $\alpha$  is the coefficient of thermal expansion, and  $\nu$  is the kinematic viscosity. We define dimensionless fluid flow velocities  $(u_r, u_\phi, u_z)$  and dimensionless temperature fields  $T$  and  $T_s$  in the melt and crystal, respectively. The unperturbed fluid flow velocity is in the  $z$ -direction and is a function of  $r$  alone; similarly the unperturbed temperature fields are functions of  $r$  alone.

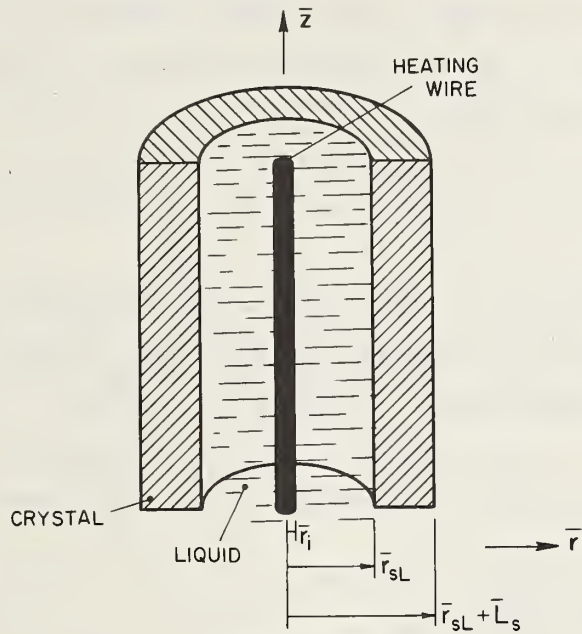


Fig. 2. Schematic illustration of the cylindrical geometry.

We decompose the fluid velocities, temperature fields, and crystal-melt interface shape  $r_I$  into an unperturbed and perturbed part, and assume that the  $\phi$ ,  $z$ ,  $t$  dependences of the perturbed quantities are of the form  $F(\phi, z, t) = \exp [in\phi + i\omega z + \sigma t]$ , where  $n$  is an integer,  $\omega$  is a spatial frequency, and  $\sigma = \sigma_r + i\sigma_i$  is a complex number which determines the temporal behavior of the system. If  $\sigma_r > 0$  for any value of  $n$  and  $\omega$ , the system is unstable. We write

$$u_r = W_r(r)F,$$

$$u_\phi = W_\phi(r)F,$$

$$u_z = u_{z0}(r) + W_z(r)F,$$

$$T = T_0(r) + T(r)F,$$

$$T_s = T_{os}(r) + T_s(r)F,$$

$$r_I = 1/(1-\kappa) + \delta F,$$

where the subscript 0 denotes unperturbed quantities, and  $\delta$  is the amplitude of the perturbation of the solid-melt interface. The unperturbed fluid velocity is given by [13]

$$u_{z0}(r) = \{c_1[\rho^2-1 + (1-\kappa^2)\ln\rho/\ln\kappa] - 4(\rho^2-\kappa^2)\ln\rho/\ln\kappa\}/\{16(1-\kappa)^2\},$$

with  $c_1 = \{(1-\kappa^2)(1-3\kappa^2) - 4\kappa^4\ln\kappa\}/\{(1-\kappa^2)^2 + (1-\kappa^4)\ln\kappa\}$  and  $\rho = (1-\kappa)r$ .

The unperturbed velocity vanishes at the inner cylinder,  $r = \kappa/(1-\kappa)$ , and at the unperturbed crystal-melt interface,  $r = 1/(1-\kappa)$ . In addition, the net flow vanishes, i.e., the integral of  $ru_{z0}(r)$  from  $r = \kappa/(1-\kappa)$  to  $r = 1/(1-\kappa)$  is zero. The unperturbed temperature fields are given by

$$T_o(r) = T_e + \ln\rho/\ln\kappa$$

$$T_{os}(r) = T_e + (k_L/k_S)\ln\rho/\ln\kappa,$$

where  $T_e$  is the dimensionless temperature of the unperturbed crystal-melt interface, and  $k_L$  and  $k_S$  are thermal conductivities of liquid and crystal, respectively (we assume that the unperturbed crystal is neither freezing nor melting).

We keep only terms linear in the perturbation quantities ( $W_r, W_\phi, W_z, T, T_s$ , and  $\delta$ ); the fluid dynamical and temperature equations are then (in the Oberbeck-Boussinesq approximation with viscosity and thermal diffusivity assumed constant)

$$(D^*D-A)W_z - \frac{1}{2}G(f+g)(Du_{z0}) + T - i\omega p = 0 \quad (1a)$$

$$D^*(f+g) + (n/r)(f-g) + 2i\omega W_z = 0 \quad (1b)$$

$$(n/r)D^*(f-g) + A(f+g) + 2Dp + 2i\omega DW_z = 0 \quad (1c)$$

$$(D^*D-A_T)T - \frac{1}{2}PG(f+g)(DT_o) = 0 \quad (1d)$$

$$[D^*D-A + (2n-1)/r^2]g - Dp - (n/r)p = 0 \quad (1e)$$

$$(D^*D-A_{Ts})T_s = 0 \quad (1f)$$

where  $D = \partial/\partial r$ ,  $D^* = D + (1/r)$ ,

$$A = (n^2/r^2) + \omega^2 + i\omega Gu_{oz} + \sigma,$$

$$A_T = (n^2/r^2) + \omega^2 + P(i\omega Gu_{oz} + \sigma),$$

$$A_{Ts} = (n^2/r^2) + \omega^2 + P_s \sigma.$$

The function  $p$  is the radial part of the perturbed dimensionless pressure,  $f = W_r + iW_\phi$ ,  $g = W_r - iW_\phi$  [15],  $G = g\alpha L^3 \Delta T / \nu^2$  is the Grashof number,  $P$  is the Prandtl number (ratio of kinematic viscosity to thermal diffusivity  $\kappa_L$  of the melt), and  $P_s = P\kappa_L/\kappa_s$  with  $\kappa_s$  the thermal diffusivity of the solid. The temperature field  $T_s$  in the solid can be expressed in terms of Bessel functions of order  $n$  with complex argument. The remaining equations for the fluid variables are equivalent to a system of eight first-order equations for  $W_z$ ,  $DW_z$ ,  $f$ ,  $p$ ,  $g$ ,  $Dg$ ,  $T$ , and  $DT$ . For  $n = 0$ , we have  $W_\phi = 0$ ,  $f = g$ , and equations (1b-c) are equivalent to equation (1e) so there are six first-order differential equations in the variables  $W_z$ ,  $DW_z$ ,  $f$ ,  $p$ ,  $T$ , and  $DT$ .

The boundary conditions at the inner cylinder are the usual no slip and no normal flow; we take the temperature as constant, so that the perturbed temperature vanishes. Thus, at  $r = \kappa/(1-\kappa)$  we have

$$W_z = f = g = T = 0 \quad (2)$$

The boundary conditions at the crystal-melt interface  $r_I$  are the usual solidification boundary conditions [6,8]. The no slip condition holds and the normal flow is such as to balance the density change on solidification. The temperature is continuous across the crystal-melt interface and is equal to the equilibrium temperature which depends on interface curvature through the

Gibbs-Thomson equation. The net heat flux at the interface balances the evolution of latent heat due to interface motion.

It is desirable for numerical purposes to set the boundary conditions at the unperturbed interface rather than at the actual crystal-melt interface. This is easily done in linear theory since any function, e.g.,  $f(r)$ , evaluated at  $r_I = r_{I0} + \delta F$  can be written as  $f(r_I) = f(r_{I0}) + (\partial f/\partial r)\delta F$ , where  $r_{I0} = 1/(1-\kappa)$  and the partial derivative is evaluated at  $r = r_{I0}$ . Again, for numerical purposes, it is desirable to eliminate  $T_s$  and  $\delta$  from the boundary conditions and write them in terms of  $W_z$ ,  $f$ ,  $g$ , and  $T$ . When this is done, we have the following linear, homogeneous, boundary conditions at the unperturbed crystal-melt interface

$$\frac{1}{2}a_1(f+g) + \varepsilon\sigma T = 0 \quad (3a)$$

$$f - g = 0 \quad (3b)$$

$$a_1 W_z + (Du_{z0})GT = 0 \quad (3c)$$

$$-a_2 T + a_1(k_L/k_S)(DT) = 0, \quad (3d)$$

where  $\varepsilon = (\rho_S/\rho_L)-1$  with  $\rho_L$  and  $\rho_S$  the density of melt and crystal, respectively,

$$a_1 = \gamma\{[(n^2-1)/r_{I0}] + \omega^2\} - G(DT_0),$$

with  $\gamma = T_M \Gamma g \alpha \bar{L}^2 / v^2$ , where  $T_M$  is the melting point of a planar interface and  $\Gamma$  is the ratio of crystal-melt surface tension and latent heat,  $H_V$ , per unit volume,

$$a_2 = \{(DT_s)/T_s\}\{a_1 + G(DT_0)[1-(k_L/k_S)]\} - \Lambda\sigma,$$

with  $\Lambda = H_V g \alpha \bar{L}^3 / (k_S v)$ . We assume that the outer radius of the crystalline annulus is maintained at a fixed temperature so that the perturbed temperature vanishes, i.e.,

$$T_s(r_{I_0} + L_s) = 0. \quad (4)$$

The ratio  $(DT_s)/T_s$ , evaluated at  $r_{I_0}$  and appearing in the definition of  $a_2$ , can be expressed in terms of Bessel functions.

For succinonitrile, it is an excellent approximation to take the thermal properties of liquid and crystal equal, i.e.,  $k_L = k_s$  and  $P = P_s$ . Further, it is reasonable (and numerical calculations have verified) that the density change upon solidification and the effect of the crystal-melt surface tension are not important. Thus, setting  $k_L = k_s$ ,  $\epsilon = 0$ , and  $\gamma = 0$ , the boundary conditions, equations (3a-d), reduce to the following:

$$f = g = 0, \quad (5a)$$

$$- (DT_o)W_z + (Du_{zo})T = 0, \quad (5b)$$

$$\{[(DT_s)/T_s] + \Lambda\sigma/[G(DT_o)]\}T - DT = 0. \quad (5c)$$

We note that if the coefficient of  $T$  in equation (5c) is sufficiently large, then the above boundary conditions further reduce to  $f = g = W_z = T = 0$ , which are identical to those at a rigid boundary (see eq. (2)).

The numerical methods used to solve the linear eigenvalue problem defined by the differential equations [eqs. (1)] and the boundary conditions [eqs. 2-4] are similar to those previously described [8]. We set  $\sigma_r = 0$ , and vary  $G$  and  $\sigma_i$ , keeping all other parameters constant, until we find a solution of the differential equations satisfying the boundary conditions. The program SUPORT [16] is used to solve the differential equations and the program SNSQE [17] is used for the non-linear iteration procedure. For the case of rigid boundaries, we have compared our results for  $G$  and  $\sigma_i$  with  $n = 0$  and  $P = 15$  to those of Table 1 of Choi and Korpela [13], who used a quite different numerical method; there is agreement to about 1%.

## NUMERICAL RESULTS

We present results for physical properties appropriate to succinonitrile for a radius ratio  $\kappa = 0.02$ . We take  $\bar{L} = 0.25$  cm, and  $L_s = 1$ ; for succinonitrile [19] we have  $P = P_s = 22.8$ ,  $\epsilon = 0.0283$ ,  $\gamma = 4.53 (10^{-4})$ ,  $\Lambda = 1.017 (10^4)$ , and  $k_L/k_s = 1.0$ . The Grashof number as a function of the spatial frequency  $\omega$  is shown in Figure 3. We have found three distinct modes of instability, two axisymmetric modes ( $n = 0$ ) and an asymmetric mode ( $n = 1$ ). The lowest mode is asymmetric with a minimum at  $\omega = 1.35$  with  $G = 176$  and  $\sigma_i = -0.977 (10^{-2})$ . The lower symmetric mode has a minimum at  $\omega = 1.45$  with  $G = 464$  and  $\sigma_i = -3.65(10^{-2})$ , whereas the higher symmetric mode has a minimum at  $\omega = 2.3$  with  $G = 2152$  and  $\sigma_i = -43.7$ . If we take  $\gamma = \epsilon = 0$ , the values of  $G$  and  $\sigma_i$  change by less than 0.1%. For the remaining discussion we assume  $\gamma = \epsilon = 0$  so that the boundary conditions at the unperturbed crystal-melt interface, equation (3), reduce to equation (5). The higher symmetric mode in Figure 3 is identical to that obtained if the crystal-melt interface is replaced by a rigid isothermal boundary, i.e., replace the crystal-melt boundary conditions, equation (5), with equation (2). For this mode, in fact, equation (5) approximately reduces to equation (2) since the factor multiplying  $T$  in equation (5c) is very large compared to unity, and hence  $T \approx 0$  at the solid-melt boundary. Since with  $\gamma = 0$ ,  $\delta = -T/(DT_0)$ , it follows that there is very little interface deformation in this mode.

In contrast the lower axisymmetric and the asymmetric mode only occur when a crystal-melt boundary is present. For these modes the coefficient of  $T$  in equation (5c) is a complex number of order unity so that  $T$  and  $DT$  become the same order of magnitude. In turn,  $W_z$  does not vanish at the unperturbed crystal-melt interface [see eq. (5b)].

For the remaining discussion we call the higher symmetric mode the "convective mode" since it involves little interface deformation and occurs when a rigid boundary is present. The lower symmetric and the asymmetric mode which would not occur in the absence of either fluid flow or the crystal-melt interface will be denoted as "coupled modes." We define a dimensionless wave velocity  $s = -\sigma_i/(G\omega)$  in units of  $(\nu G/\bar{L}) = 0.104G$  cm/s so that positive  $s$  indicates

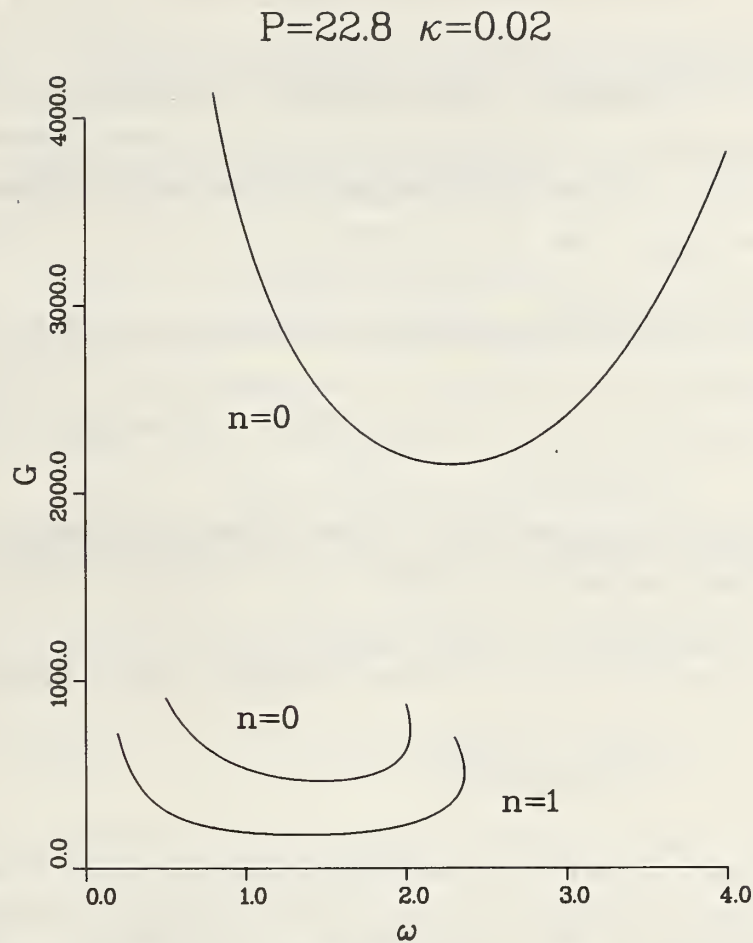


Fig. 3. The Grashof number at the onset of instability as a function of the spatial frequency  $\omega$  of a sinusoidal perturbation. The  $n = 0$  modes are axisymmetric while the lowest mode ( $n = 1$ ) is asymmetric.

waves traveling upwards. The maximum unperturbed flow velocity is  $8.2 \cdot (10^{-3})$ ; the wave speeds are  $8.8 \cdot (10^{-3})$ ,  $5.4 \cdot (10^{-5})$ , and  $4.1 \cdot (10^{-5})$  for the convective, coupled symmetric, and coupled asymmetric modes, respectively. The wave speed for the convective mode is approximately the same as the maximum flow velocity [13], whereas the wave speed for the coupled modes are two orders of magnitude smaller than the maximum flow velocity. It is interesting that the crystal-melt transformation, which involves both melting and freezing with latent heat absorption and evolution, can only follow the relatively slow fluid motions of the coupled mode.

We have carried out additional computations with  $\sigma_r \neq 0$  to estimate how rapidly instability develops. With  $\sigma_r = 2 (10^{-3})$ , the asymmetric coupled mode has a minimum at  $\omega = 1.4$  with  $G = 205$  and  $\sigma_i = -1.06 (10^{-2})$ . This Grashof number is 16% above the critical Grashof number at the onset of instability; the perturbation amplitudes would increase by an order of magnitude in a time of  $1.15 (10^3) [2.77 (10^3) \text{ s} = 46 \text{ min}]$ . Thus, it takes a relatively long time for the instability to develop. Further, calculations indicate that the dimensional time for an instability to develop is roughly proportional to  $\bar{L}^5$ . Even  $\bar{L} = 1 \text{ cm}$  would result in such a slow development of the instability as to be unobservable over several days.

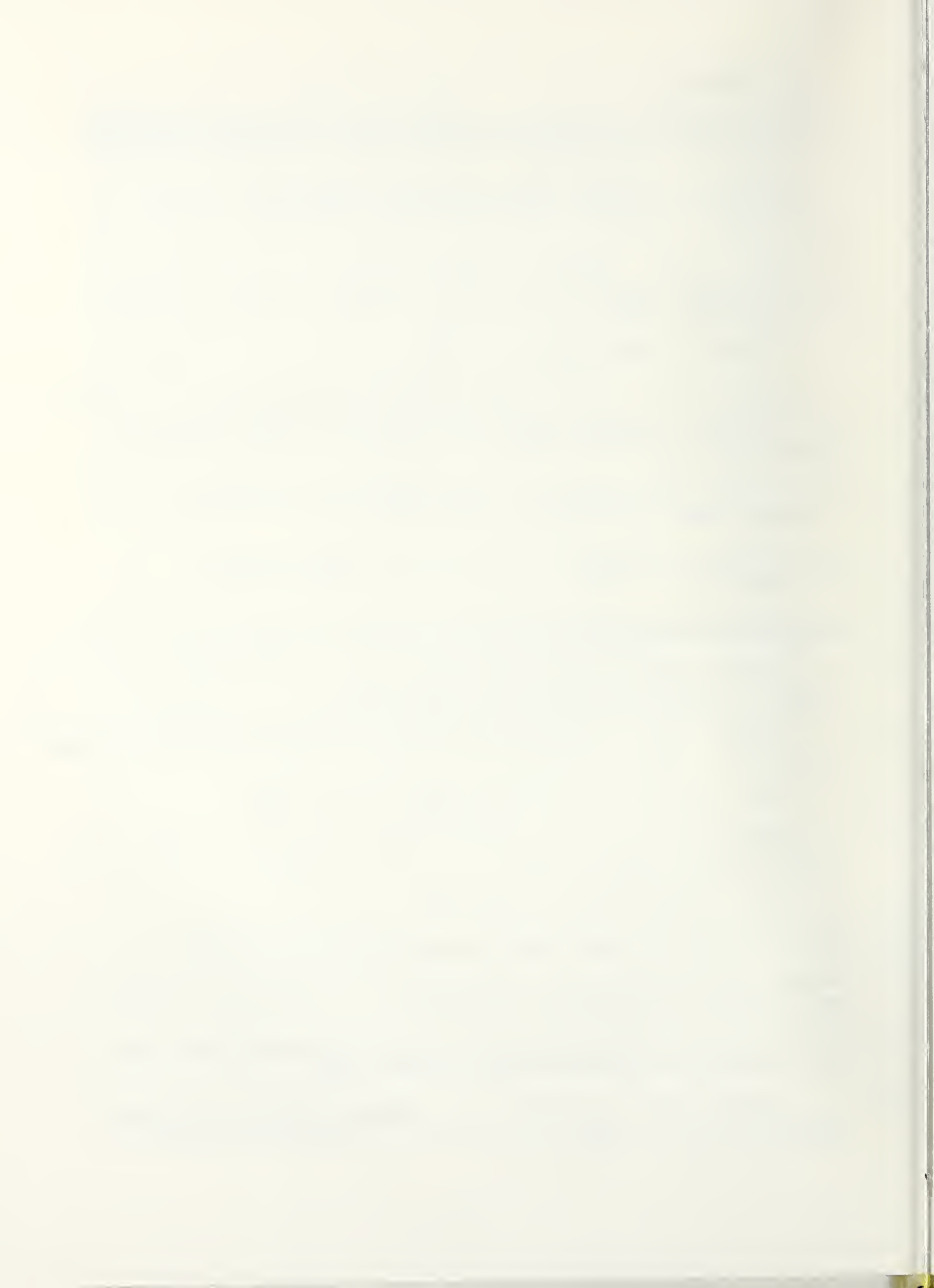
A more detailed study over a wider parametric range will be presented in a future publication. We remark that the coupled mode of instability occurs for planar solid-melt interfaces, e.g., let  $\kappa \rightarrow 1$ . In this case, of course, there is no distinction between symmetric and asymmetric modes.

#### ACKNOWLEDGMENTS

The authors gratefully acknowledge the support of this investigation by the Materials Processing in Space Program, National Aeronautics and Space Administration. We also thank Drs. S. H. Davis, S. Ostrach, R. G. Rehm, D. A. Saville, R. F. Sekerka, and J. A. Simmons for helpful discussions.

## REFERENCES

1. J. R. Carruthers, in: Preparation and Properties of Solid State Materials, Vol. 3, eds. W. R. Wilcox and R. A. Lefever, Dekker, New York, 1977, p. 1.
2. D.T.J. Hurle, in; Current Topics in Materials Science, Vol. 2, eds. E. Kaldis and H. J. Scheel, North-Holland, Amsterdam, 1977, p. 549.
3. S. M. Pimputkar and S. Ostrach, J. Crystal Growth 55, 614 (1981).
4. P. G. Drazin and W. H. Reid, Hydrodynamic Stability, Cambridge University Press, Cambridge, 1981.
5. J. S. Langer, Rev. Mod. Phys. 52, 1 (1980).
6. S. R. Coriell and R. F. Sekerka, PhysicoChemical Hydrodynamics 2, 281 (1981).
7. R. T. Delves, in: Crystal Growth, Vol. 1, ed. B. R. Pamplin, Pergamon, Oxford, 1974, p. 40.
8. S. R. Coriell, M. R. Cordes, W. J. Boettinger, and R. F. Sekerka, J. Crystal Growth 49, 13 (1980).
9. S. R. Coriell, M. R. Cordes, W. J. Boettinger, and R. F. Sekerka, Adv. Space Res 1, 5 (1981).
10. J. I. Mickalonis, M. S. Thesis, Materials Engineering Department, Rensselaer Polytechnic Institute, Troy, New York (1982).
11. M. E. Glicksman and J. I. Mickalonis, Proceedings of the 16th Southeastern Seminar on Thermal Sciences, Miami, Florida, 1982.
12. G. Z. Gershuni and E. M. Zhukhovitskii, Convective Stability of Incompressible Fluids, Keter, Jerusalem, 1976.
13. I. G. Choi and S. A. Korpela, J. Fluid Mech. 99, 725 (1980).
14. A. H. Shaaban and M. N. Ozisik, 7th International Conference of Heat Transfer, Munich, Germany, 1982.
15. V. K. Garg, J. Fluid Mech. 110, 209 (1981).
16. M. R. Scott and H. A. Watts, SIAM J. Numerical Anal. 14, 40 (1977).
17. SLATEC Common Math Library, The Program SNSQE was written by K. L. Hiebert and is based on an algorithm of Powell [18].
18. M.J.D. Powell, in: Numerical Methods for Nonlinear Algebraic Equations, ed. P. Rabinowitz, Gordon and Breach, New York, 1970.
19. R. J. Schaefer and M. E. Glicksman, in: Modeling of Casting and Welding Processes, eds. H. D. Brody and D. Apelian (The Metallurgical Society of AIME, Warrendale, PA, 1981) p. 375.



### Task 3

## Measurement of High Temperature Thermophysical Properties of Tungsten Liquid and Solid

D. W. Bonnell  
Materials Chemistry Division  
Center for Materials Science

### SUMMARY

With the end of phase two experiments, it has been necessary to reassess strategy and consider alternative experimental approaches. The most promising immediate line has been identified as improving the mechanics of calorimeter operation. A complete plan for achieving this improvement has been proposed, and a subset of the proposal implemented. Actual testing of the new design has been carried out and was quite successful, with 12 samples being successfully dropped, four in a nearly molten state. Only one correctable fault in the gate linkage was found and is being rectified.

A new procedure has been developed for fabricating samples which is less expensive and more convenient. About 20 samples are now available. This method of fabrication was developed in NBS' shops and consists of a grinding process to give clean spheroidal specimens  $\sim 1.25$  cm in diameter. The larger sample has been tested successfully at GE. The larger samples are expected to provide improved stability.

A complete system automation plan has been developed which will act as a model for future flight based systems as well as being a guide for improvements to the current system. Details of timing, required hardware and computer devices are discussed, and a sketch of software requirements is given.

Current plans are to schedule a new experimental series as soon as possible. Rice is bringing a new student on board who has already been acquainted with the experimental problems and apparatus.

## INTRODUCTION

The evaluation of experimental procedures used in the interaction between the General Electric Advanced Applications Laboratory (GE) and Rice University (Rice) to measure high temperature enthalpy increments for liquid and solid tungsten has been the primary aim of this task. Coupling of GE's unique apparatus [Wouch, 1978] for levitating and melting tungsten with Rice's expertise in high temperature measurements with isoperibol calorimeters used in conjunction with levitation heating [Chaudhuri, et al., 1970; Treverton and Margrave, 1971 a, b; Bonnell, 1972] has been expected to provide the means to measure hertofore estimated thermophysical properties of tungsten.

The location of tungsten at the extreme upper end of the melting point scale of metals and elements provides a unique point for any correlation. Currently, questions such as the nature of the liquid state heat capacity function, or even values of liquid heat capacity, are only answered by estimates. A review of the state of experimental data for the heat of fusion of tungsten [Bonnell, 1981] indicates the best value is still uncertain by perhaps 50 percent, not significantly better than an estimate.

A variety of theoretical, correlative and practical applications await directly measured reliable data for the fundamental thermodynamic quantities of heat content and heat and entropy of fusion for tungsten. The importance of this effort, in spite of experimental difficulty, is still clear. The difficulty of measurement by any technique is well recognized. This effort represents the dividing line between experiments which can be performed in the terrestrial environment, and those which require the advantage of no gravity to accomplish.

## DISCUSSION

Details of the plan for automation are now in a condition where an integrated approach is clear and natural. The component areas are: (1) pyrometer; (2) window correction; (3) calorimeter data acquisition; (4) calorimeter operation; and (5) RF and e-beam power. The techniques for accomplishing items (1) and (2) have been developed and reported on earlier [Bonnell, 1981]. Although it is probable that some version of that system will be necessary to obtain precise temperatures above the melting point of tungsten, we anticipate the majority of data will be obtained at the melting point in the next series of experiments and we have adequate techniques for hand correcting individual drops. Experience has shown, however, that manual multicolor pyrometry is not feasible with this system, and brightness temperatures will be the prime mode of temperature determination.

Due to more serious problems, the actual implementation of the pyrometry automation has been deferred [Frost and Stockoff, 1981]. A major problem is the inability to control the sample, as it liquifies, well enough to provide a controlled drop into the calorimeter. In a few instances, when the calorimeter was not attached, it has been possible to liquify tungsten. This is a dynamic process, requiring a skilled operator to balance heating rate (as power input from the e-beam heating system) and flotation point in the coil. Recovered melted samples were resolidified as soon as molten. A sample was melted recently which, on inadvertant release, fell to the bottom of a 1 meter drop tube and splashed, giving a myriad of tiny spherules. This event establishes the feasibility of the experiment, and answers the question of whether liquid drops can be made. The analysis is based on an integrated form of the radiative loss.

Assume the sample is a body of surface area  $A$  and total hemispheric emissivity  $E_T$ . At a temperature  $T$ , the radiative heat loss for the sample,  $dH_r^*$  during time  $dt$  is given by the Stephan-Boltzman law as

$$dH_r^* = E_T A \sigma T^4 dt \quad (1)$$

where  $\sigma = 5.67032 \times 10^{-12}$  joule  $\text{sec}^{-1} \text{cm}^{-2} \text{K}^{-4}$  ( $1.35524 \times 10^{-12}$  calorie  $\text{sec}^{-1} \text{cm}^{-2} \text{K}^{-4}$ ) [Cohen and Taylor, 1973] is the Stephan-Boltzman radiation constant. The correction to (1) due to the fact that radiation actually occurs to non-zero temperature surroundings is less than one part in  $10^5$  above 3000 K and will be ignored. Let  $C_p^*$  be the total constant pressure heat capacity for a sample of mass  $m$ . Then

$$dH_r^* = -C_p^* dT \quad (2)$$

Combining (1) and (2) gives, on rearrangement

$$dt = \frac{C_p^*}{A \sigma E_T} \cdot \frac{dT}{T^4} \quad (3)$$

Now assume that  $C_p^*$  is independent of temperature and that there are no temperature gradients in the body. The first assumption is consistent with all experimental evidence for liquid refractory metals. The second is reasonable for liquids, in view of the electromagnetic stirring of the melt and good thermal conductivity of the sample. This should not cause an error of more than a few percent even where (as in levitated solids) noticeable gradients ( $\sim 50$  K) have been observed. With the initial conditions that at  $t = 0$ ,  $T = T_0$ , the initial sample temperature, (3) may be integrated from  $T_0$  to  $T$  corresponding to time from 0 to  $t$ .

Solving for the final temperature gives

$$T = \left[ \frac{C_p^* T_o^3}{3E_T A \sigma t T_o^3 + C_p^*} \right]^{1/3} \quad (4)$$

Equation (4) can be substituted into (2) to give the total heat loss,  $\Delta H_r^*$ , in time  $t$  as

$$\Delta H_r^* = C_p^* T_o \left[ 1 - \left( \frac{1}{1+y} \right)^{1/3} \right] \quad (5)$$

where

$$y = \frac{3E_T A \sigma t T_o^3}{C_p^*} \quad (6)$$

The expression in brackets in (5) may be expanded by the binomial formula as

$$\left[ 1 - \left( \frac{1}{1+y} \right)^{1/3} \right] = 1/3y - 2/9y^2 + 13/81y^3 \dots \quad (7)$$

Taking only the leading term of this expression, equations (5) and (6) reduce to

$$\Delta H_r^* \approx 1/3y C_p^* T_o \equiv E_T A \sigma t T_o^4 \quad (8)$$

which is the integral of (1) assuming constant temperature.

From equation (4), we can estimate the degree of undercooling achievable with the G. E. apparatus. The sample was  $\sim 10$  gms of 17.6 gm/cc [Smithells and Brandes, 1976] tungsten. The drop distance is  $\sim 1$  meter ( $t \approx 0.45$  sec).  $C_p^*$  is 0.46 calories assuming the Hultgren, et al [1973] estimate for  $C_p(1) = 8.5 \text{ cal mole}^{-1} \cdot \text{K}^{-1}$ . This estimate may be in error by 10-20 percent or more, but should not lead to an erroneous conclusion in this case. The minimum temperature at drop is the melting point of

tungsten. The value of Cezairliyan [1972] of 3695 K is the current best estimate for  $T_m$  (tungsten) and is considered more reliable than the JANAF [1966] value. This value is in excellent agreement with the average of investigations since 1960 [Cezairliyan, 1972]. The value of  $E_T$  is estimated by extrapolation from data reviewed by Smithell [Smithell and Brandes, 1974]. With these data  $T_{final}$  is obtained from equation (4) as 3476 K, an under cooling of  $\sim 6$  percent. This is certainly a reasonable value, well within accepted limits of supercooling [Perepezko, 1980]. This estimate ignores other loss modes, such as conduction (negligible in vacuum) and material loss due to vaporization. The largest error (except for  $C_p$  and  $E_T$  uncertainty) is an over-estimation in the assumption of sphericity, which is considered to be negligible.

#### CALORIMETER OPERATION

The data acquisition system currently attached to the calorimeter is a reasonable stand-alone system. With its interface, it provides 300 Baud RS232 serial output of the six digit temperature of the calorimeter block at the thermometer's clocked update period. The format was carefully designed to allow direct acquisition and use by a teletype-like device or to allow interfacing to a computer port.

The calorimeter gate mechanisms have been the subject of development in the past year. When it became clear that manual operation would not achieve a successful liquid drop except by extreme good fortune, alternatives were considered. Figure 1 shows a sketch of proposed modifications to the calorimeter jacket and shield assembly to solve this problem. The salient features are (1) an optical drop detection technique; (2) passive optical and electron beam shielding; (3) a power-actuated radiation shield; (4) an extension of the calorimeter jacket to

behave as a shield, with a thermometer to detect failed drops; (5) a power-actuated block gate, (6) and a thermal shunt mechanism.

The optical drop detector is the prime item in the system. The choice of optical detection was made because it seemed to impose the least restrictions on future samples while retaining the non-contact qualities of levitation. The primary problem anticipated was the fact that a tungsten sample is radiating more than 1000 watts at its melting point, with a substantial portion in the near IR and visible. The movement of the sample causes considerable flickering in the chamber. Even with good collimation, it was unclear how likely false triggering would be with a simple photo-diode detector. One possibility would be to provide an optical trap encompassing the field of view of the diode as suggested in figure 1. A second effort suggestion was the use of an ordinary interrupted light beam, encoding the light beam by modulating it at a relatively high frequency (ca. 1-10 KHz). Then detection by a synchronous detector would provide the necessary isolation. This is, however, a relatively expensive and complex solution, and the simpler one would be preferred. The actual implementation at GE utilized a 4 mm glass light pipe with a small tantalum nose piece shaped to give a roughly horizontal slit entrance aperture. The opening is located below the work coil and is shaded from the sample by it. Bench tests implied that this arrangement would yield a signal to noise trip point of the order of 10:1. That is to say, if a sample at  $T_m$  (tungsten) = 3695 K is the selected trip point, the trigger would not trip to a light source from a sample at a temperature below  $\sim 2500$  K, and the sample would have to be at a temperature of 5000 K, before stray light would trip the trigger. To achieve this rejection, it was necessary to shield the light pipe from grazing light which actually constituted the most serious

spurious trigger source. Mr. Brian Stephenson of Rice and myself did the final testing and adjustment of this device at GE. A direct map of the apparatus' response to a bench light source was done to set the trip relative to that lamp. Since the required gain change for the tungsten experiments required decrease in sensitivity of the order of 1000-fold, it was necessary to investigate the circuit gain function to center the response at the desired temperature. The grazing incidence light response problem was solved by an overlapping spiral wrap of copper foil on the light pipe. A series of tests were carried out on the trip mechanism in situ with actual tungsten samples. In 12 drops, the mechanism tripped at each drop and never false triggered.

The original gate suggestions (see figure 1) recommended rotating gates driven by springs with a solenoid and pawl mechanism to release the gates. The time between drop detector actuation and arrival of the sample at the calorimeter is  $\sim 0.3$  second. The available distance to the first gate location cuts this time to  $\sim 0.1$  second. A rotating gate is the simplest way to achieve such short opening times without large forces. However, GE, using commercial rotary solenoids, devised an entirely different operating mechanism, which involved only the single existing single mechanical feedthrough and operated both gates with a single linkage. The available torque from the rotary solenoid is high enough to open both gates in the necessary time. The problems with this design are (1) a thermal isolation element must be part of the gate linkage and (2) the drop-leaf operation of the main radiation gate does not allow the extension of the jacket above the calorimeter as a collimating shield. (See figure 1). The live tests showed that the thermal isolation link was a weak design point. GE is now redesigning this

item. The collimating shield is probably not absolutely essential, and the shield mechanism for the gate provides some protection. Further testing will be required to determine if heat from this source is a problem. The additional problems in getting the design of Figure 1 sequencing properly is a good argument for the redesign. Mr. Daniel Rutecki of GE is to be complemented on his ingenuity and understanding of the requirements of the situation in converting my initial design into working hardware.

The entire new system has been tested for functionality at GE with tungsten samples at the melting point. Four samples were partially molten, and one, which was held momentarily at liquefaction appeared to have been more than 80 percent molten on inadvertant loss. This success is as good as all our previous efforts, and represents a success ratio very much higher than any previous effot.

The rest of the features of the design of figure 1 have not yet been implemented. The thermal shunt deserves some mention. A significant problem in high temperature drop calorimetry is cycling the system. Where vacuum insulation is concerned, the drift rate of the calorimeter must require hours to return to starting conditions. Normally, this is not a problem, as it is necessary to dismount the calorimeter to weigh the dropped specimen. It is a simple matter to adjust the block to starting temperature conditions at this time. However, in this system, a failed drop requires dismounting as well, just to avoid this several hour wait. Under the best of conditions, a run requires about two hours from drop to dismount. Dismount time is about one hour. A high conductance thermal link which could be made between the jacket and block could shorten this three hour turnaround considerably in the case of

failed drops. In the design shown, it also seems feasible to incorporate the post drop weighing process with the thermal shunt. If the thermal shunt contained a sensitive load cell, it would be possible to lift just the cup to obtain the weight. Commercial vendors exist who can supply remote weighing devices with the necessary 1 mg or better sensitivity for loads of more than the  $\sim 200$  gm of the sample cup. These features are considered highly desirable in the fully automated system.

#### SYSTEM AUTOMATION

Figure 2 shows a block schematic of the suggested automated computer system. This is a straight-forward automation problem which should be implemented with off-the-shelf hardware. From the hardware viewpoint, the external input/output (I/O) structure is most important. Figure 2 breaks this down to the signal level and organizes it in terms of I/O types. Analog input signals are characterized by resolution and digitizing speed. The only signal requiring any real speed is OBJECT DETECTOR INTENSITY and then only if computer software is to replace the comparator logic currently being used. Assuming the detector is located 1.5 cm below the sample levitation coil, the sample will be in the view point of the detector for  $\sim 0.016$  sec while falling. Assuming several observations are necessary to trigger reliably, a sampling rate of  $\sim 250$  Hz is required. The PYROMETER SIGNAL is updated at the camera frame rate,  $\sim 30$  Hz [see Bonnell, 1981 for details]. The maximum resolution required is in JACKET TEMPERATURE and PYROMETER SIGNAL. The amplifiers and track and hold for the PYROMETER SIGNAL need be stable to no better than 1:2000, so twelve bit bipolar digitization is more than adequate. These requirements are now well within the state-of-the-art for monolithic analog-to-digital converters. In fact, a single multiplexed converter such as the Analog Devices AD363 system [Analog Devices,

1980] a 16 channel multiplexed, 30 KHz, 12 bit system, is quite adequate. Assuming a computer with a 32 bit word (and instruction cycle time) of one MHz, and an interrupt driven I/O routine of 100 instructions and overhead of 12 instructions per interrupt, all seven channels can be serviced at a 1 KHz rate utilizing only twenty percent of machine capacity. Having the OBJECT DETECTOR INTENSITY input to, say channel 0 and 4, a sample rate of 1 KHz for eight channels causes the OBJECT DETECTOR INTENSITY to be sampled at 250 Hz, and all other signals at 125 Hz. This would require a 16 bit (or 2-8 bit) bidirectional parallel port to handle channel addressing, hand shaking and transfer, and a real-time timer to clock the acquisition. The assumption of 100 instructions for the I/O loop assumes a self triggered acquisition system. A considerable safety factor is included in these estimates, as this sampling rate would provide ~40 samples over the falling ball, and four readings of each sample of the pyrometer.

The Parallel I/O channel is used for reference and control information. Eight aperture sizes and eight band pass filters is quite adequate to provide multicolor pyrometry for the temperature range required. A simple binary coded switch on the APERTURE SIZE and the FILTER # shafts (see Bonnell, 1981 for pyrometer system details) provide absolute position indication with no operator initialization. INDUCTION HEAT STATE and ELECTRON BEAM STATE are indicators as to the on/off status of the two heating units, allowing processing code to correct for effects due to these power sources. The SHIELD TEMPERATURE, INDUCTION POWER, and ELECTRON BEAM POWER provides for correction of the leakage rate to the calorimeter by accounting for strong e-beam and induction effects. This information will be stored with the calorimeter temperature for final

data reduction. As these effects have not been negligible in the past, corrections are necessary.

The timing on processing the parallel port is keyed to the pyrometry filter action, and should involve processing of the order of 25 percent of the A-to-D machine overhead. The Parallel I/O channels are to be processed as a task synchronous with PYROMETER SIGNAL and would be scheduled for reading on the completion of an aperture or filter change.

Stepping the aperture and filter wheels could be done directly, but the timing required is of the order of the A-to-D sample time. To be specific, if eight apertures are available and eight filters are in use, it is desirable to expect to use a different filter to acquire a different color temperature at each reading of the pyrometer signal. A 30 Hz update rate on the pyrometer signal implies a 30 Hz filter (and aperture, if necessary) change rate. Eight filters/apertures mounted on a wheel require 25 steps of a nominal 200 step/revolution stepper motor. Typical small stepping motors are capable of averaging 3000 steps/sec with proper ramping. At this rate, a filter can be changed between pyrometer reading updates. Considering the other processing expected of the computer, and the inexpensiveness of intelligent stepper drivers with firmware ramping, it is proposed to use devices such as the Cybernetic Micro System CY512 [CMS 1982] stepper system which is capable of independent automatic operation of the stepping motors. With this system each motor can be fully programmed and operated via a standard eight bit parallel port with handshake lines. An actual movement is invoked by sending a seven bit code (e.g., ASCII "D"). This is to be gated by an external enable timer started by the pyrometer frame clock and open for the dead time allowable until the stepper cannot be started

and complete the movement before the pyrometer reading is updated. This trial-and-error set up is not essential, but provides insurance in the case where changes in coding cause a running system to exceed CPU resources. When set up in this way, the interrupt routine would, on recognizing the pyrometer track and hold latch, start the task to step a filter (and aperture, as necessary), and, on checking the APERTURE SIZE and FILTER NUMBER on receipt of PYROMETER SIGNAL, determine that the filter was in place at data acquisition time. This additional code will run in interrupt mode and should easily fit in one of the eight A-to-D time slices, thus using about three percent of available CPU time at worst.

The RELAY CONTROL channel is in actuality a bit parallel port with at least four high speed "relay" closures under computer control. Speed requirements should be better than the read rate of the OBJECT DETECTOR INTENSITY, since actions such as gate release, e-beam enable, etc. may need to be accomplished in this time frame. The contacts should be capable of 1-3 amps. The functions are self explanatory, with the relays being in series with mechanical switches for INDUCTION HEAT, E-BEAM ENABLE and RADIATION GATES UNLOCK. The SAMPLE RELEASE relay parallels the manual release and a bit should be set for return by the manual switch if the sample is manually released.

The THERMAL SHUNT was discussed earlier; the actual actuating mechanism could be a solenoid, a small pneumatic or hydraulic cylinder or a mechanical linkage. The maximum throw should not need to be more than 1/2", as the calorimeter block could be hollowed out to accommodate a shaft to lift the cup for weighing. A tiny pneumatic cylinder is probably the most convenient item. Note that weighing could occur during the thermal shunt operation.

The SERIAL I/O channels are simple RS232 protocol ASCII coded channels. Each channel should be capable of any normal BAUD rate between 110 and 9600, especially to include 300 BAUD, 1200 BAUD and 9600 BAUD. All these channels will be operated interrupt driven on a character by character basis. Since input rates are very low (SYSTEM CONSOLE, 1 or 2 char/sec intermittently; CALORIMETER TEMPERATURE, 10 characters at 300 BAUD every 10 seconds; SAMPLE WEIGHT, 10 characters at 300 BAUD every experiment) the characters can be processed individually as scheduled tasks.

The above requirements indicate a minimum CPU of the Z80 class, operating at 4 MHz. Memory requirements are set by the amount of code and data, but even if a substantial portion of the background tasks are BASIC or FORTRAN, 65 K bytes should be sufficient for the system needs. An existing FORTRAN program for the post processing has been run in less than 30K bytes. An interrupt timer is required to drive the A-to-D multiplexer and a real time time-of-day clock should be available against which to log the data, as well as provide between run cycle timing. Twin 5-1/4" floppy disks will be required to store and edit data, and hold system software. A minimal hardcopy unit would be a simple low speed 80 column impact printer. Graphics capability or a plotter could be used to provide post run diagnostics, but is not essential for day to day operation. The display can be a standard alphanumeric CRT with 80 character by 24 line black and white capability. This can be the system display device under non-automation conditions. The software should keep the operating parameters indicated in figure 2 as well as a variety of status displays running, updated at scheduled intervals. The variety of microprocessor systems meeting these requirements includes most units on the market. Since extensive software development is

The SERIAL I/O channels are simple RS232 protocol ASCII coded channels. Each channel should be capable of any normal BAUD rate between 110 and 9600, especially to include 300 BAUD, 1200 BAUD and 9600 BAUD. All these channels will be operated interrupt driven on a character by character basis. Since input rates are very low (SYSTEM CONSOLE, 1 or 2 char/sec intermittently; CALORIMETER TEMPERATURE, 10 characters at 300 BAUD every 10 seconds; SAMPLE WEIGHT, 10 characters at 300 BAUD every experiment) the characters can be processed individually as scheduled tasks.

The above requirements indicate a minimum CPU of the Z80 class, operating at 4 MHz. Memory requirements are set by the amount of code and data, but even if a substantial portion of the background tasks are BASIC or FORTRAN, 65 K bytes should be sufficient for the system needs. An existing FORTRAN program for the part processing has been run in less than 30K bytes. An interrupt timer is required to drive the A-to-D multiplexer and a real time time-of-day clock should be available against which to log the data, as well as provide between run cycle timing. Twin 5-1/4" floppy disks will be required to store and edit data, and hold system software. A minimal hardcopy unit would be a simple low speed 80 col impact printer. Graphics capability or a plotter could be used to provide post run diagnostics, but is not essential for day to day operation. The display can be a standard alphanumeric CRT with 80 char by 24 line black and white capability. This can be the system display device under non-automation conditions. The software should keep the operating parameters indicated in figure 2 as well as a variety of status displays running, updated at scheduled intervals. The variety of microprocessor systems meeting these requirements includes most units on the market. Since extensive software development is involved

involved and at least six parallel ports and three serial ports are needed, the choice should be made on a basis of convenience of peripherals and availability of interrupt driven task scheduled software packages in assembly code.

The software is a non-trivial package and beyond the scope of this task to develop. However, the basic features can be sketched around the hardware design. A core interrupt routine to service the A-to-D system, the stepping motor parallel ports, the serial ports and the clocks is required. This can be vectored, but a single level polled structure should be adequate. The foreground program would be a scheduled task execution routine, which processes tasks scheduled by the interrupt routines. Typical of such scheduled tasks are (1) Process calorimeter temperature and report drift status; (2) collect current aperture size and filter, and report sample temperature(s); (3) change experiment mode to (a) initialize, (b) levitating, (c) melting, sample acceptable, (d) drop sample, (e) post drop process, (f) end of experiment; (4) Request sample weight and thermal shunt system; (5) process sample weight; (6) report system status of (a) shield temperature, (b) coating absorbance, (c) induction and e-beam power levels, (d) filter in use, etc.

As the operating system is developed, a further breakdown of the task structure will be possible. Changes, such as the current calorimeter gate automation, may significantly alter operation. The current mechanical tripping of the calorimeter makes it possible for the computer not to monitor the drop detector and removes considerable complexity from the software. The loss in generality is not yet clear, but is probably not significant.

Table 1 presents an operation scenario which details the overall progress of an automated experiment. With the controls and monitors described, the system will follow and report on each stage of the experiment without operator intervention. The only operator action required as far as the calorimeter system is concerned, will be a simple GO/NO GO decision at step 4. Step 5 can be manual or inadvertant and the result will be the same, and processing without further operator action will take place.

This automation scheme expects direct operator action to control sample processing. That is to say, an operator will externally adjust induction power and e-beam power to achieve desired results. It would be possible to include an ability to perform these actions under automatic control, but a complete video image (at least 20 x 20 pixel resolution) of the coil region should be monitored to determine sample stability, and several (at least three) 12 bit digital-to-analog outputs would be required to control the induction power and e-beam power. This additional complexity would perhaps double the size of the operating system software, and will require a processor ~five times the instruction cycle time and data fetch time of the Z80, i.e., a Motorola 68000 grade CPU or a minicomputer system. This is not a prohibitive problem, simply one which I recommend be considered after the current system functions well.

Table 1

OPERATION SCENARIO

- (1) CALORIMETER AUTOMATION IN "MONITOR MODE"
  - Dropped object detector disarmed (radiation gates are locked closed)
  - Follow initial drift
  - Notify operator when minimum drift data acquired
- (2) SAMPLE LEVITATED, STABILIZED
  - Check for influence, correct drift data, notify operator
  - Monitor induction power, sample temperature
- (3) AUXILIARY HEATING ON (ELECTRON-BEAM)
  - Check for additional heat input, monitor shields...
- (4) OUTGASSING...SATISFACTORY--ARM OBJECT DETECTOR (OPERATOR DECISION)
- (5) SAMPLE DROPS (or is dropped)
  - Object detector signals
  - Induction furnace, e-Beam off
  - Gates actuate in sequence
  - Shield monitored for BAD DROP, GO TO ERROR
  - Dropped object detector is disarmed
- (6) DATA SYSTEM ACQUIRES  $\Delta\theta$ , DETERMINES END OF RUN
- (7) GATES RESET, Visual or Other Inspection Satisfactory
  - Thermal shunt activated, mass determined
  - Store data
  - Hardcopy results...
  - Diactive thermal shunt
  - RESTART → GO TO 1
- (8) ERROR
  - Calorimeter thermal shunt actuated
  - Inspection to determine fault
  - Gates checked for operation...
  - RESTART → GO TO 7

## REFERENCES

1. Analog Devices, Inc. Data Acquisition Components and Subsystems, Norwood, MA (1980).
2. ASCII, American Standard Code for Information Interchange. American National Standards Institute (ANSI) Standard X3.4--1977.
3. D. W. Bonnell, NBSIR-81 ed J. R. Manning (1981).
4. D. W. Bonnell, "Property Measurements at High Temperatures--Levitation Calorimetry Studies of Liquid Metals", Ph.D Thesis, Rice Univ. (1972).
5. A. Cezairliyan, High Temp. Sci. 4, 248 (1972).
6. A. K. Chaudhuri, D. W. Bonnell, A. L. Ford, and J. L. Margrave, High Temp. Sci., 2, 203 (1970).
7. E. R. Cohen and B. N. Taylor, J. Phys. Chem. Ref. Data 2, 663 (1973).
8. Cybernetic Microsystems, CY512 Intelligent Stepper Motor Controller Los Altos, CA 1982.
9. R. T. Frost and E. Stockoff, private communication (1981).
10. R. Hultgren, P. D. Desai, D. T. Hawkins, M. Gleiser, K. K. Kelley, D. D. Wagman, Selected Values of the Thermodynamic Properties of the Elements, American Society for Metals, Ohio (1973).
11. JANAF Thermochemical Tables, 2nd Edition, NSRDS-NBS 37 (1971) and updates.
12. T. A. Sidorov and M. M. Mezdrogina, Fiz. Khim. Granits Razdela Kontaktiruyuschchikh Faz, ed V. Eremenko, p. 45-7, Naukova Dumka, Kiev, U.S.S.R. (1976).
13. C. J. Smithells and E. A. Brandes, Metals Reference Book, 5th edition, Butterworths, London (1976) ( $E_T$ , p. 1023) ( $\rho_m$ , p. 944).
14. J. A. Treverton and J. L. Margrave (a) J. Phys. Chem. 75, 3737 (1971). (b) J. Chem. Thermodynam. 3, 473 (1971).
15. G. Wouch, "Containerless Melting and Solidification of Metals and Alloys in the Terrestrial and Space Environment", Ph.D Thesis, Drexel Univ. (1978).

---

\*Trade names referenced in this report are provided as examples for specificity of state of the art capability in commercial devices. Such references are not intended to imply uniqueness of these devices, or the unsuitability of similar devices of another manufacturer to the applications.

**TOP VIEW**

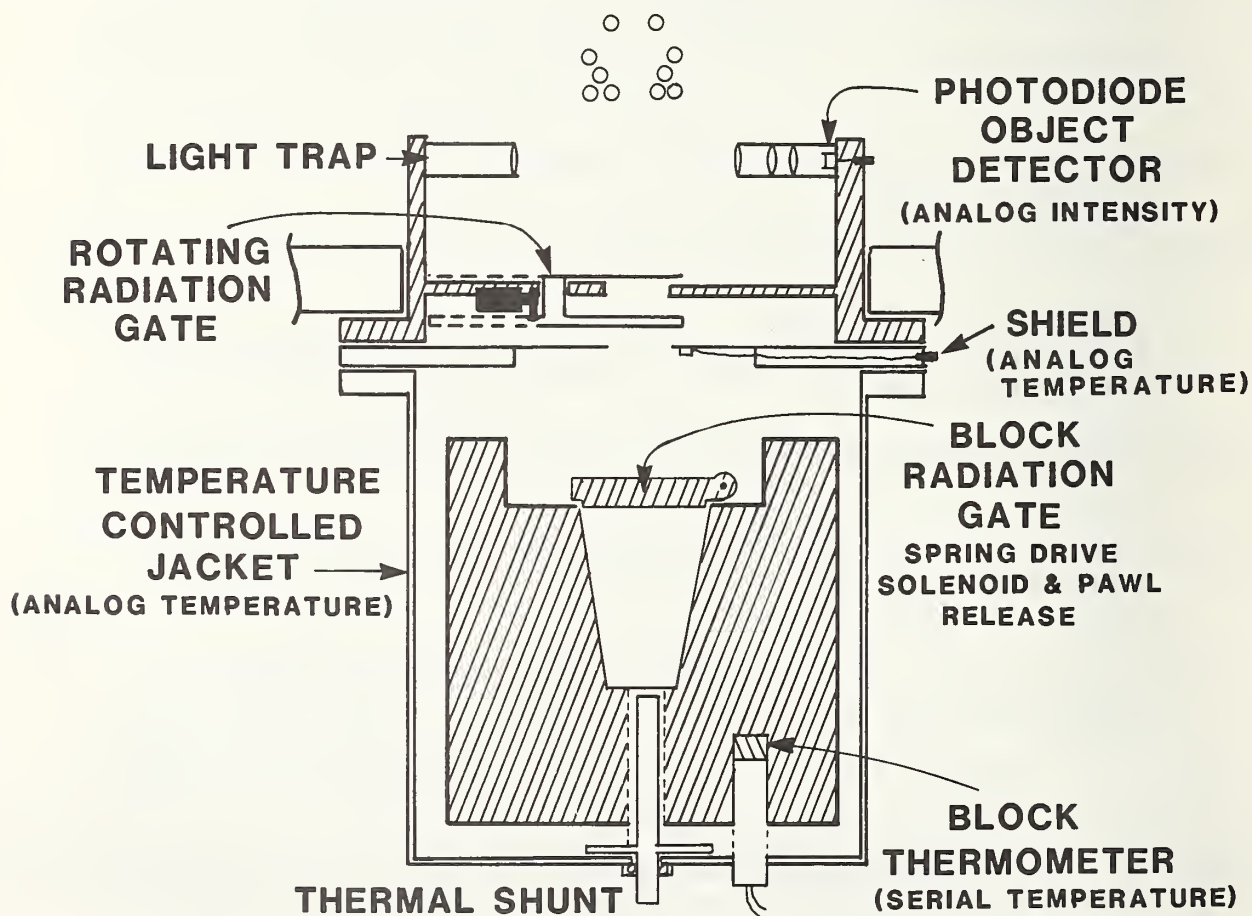
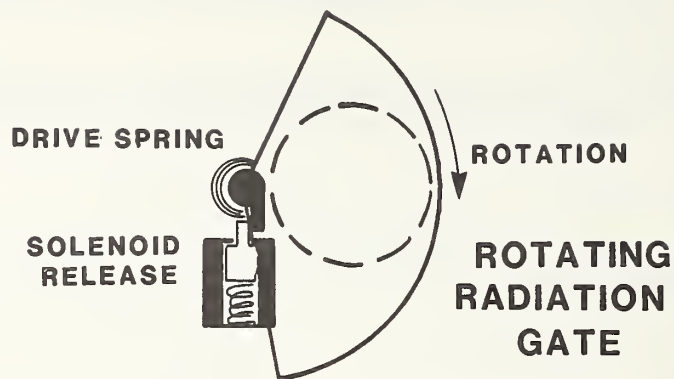


Fig. 1. Proposed calorimeter modifications to allow full automation. top view is a detail of the main rotating radiation gate assembly

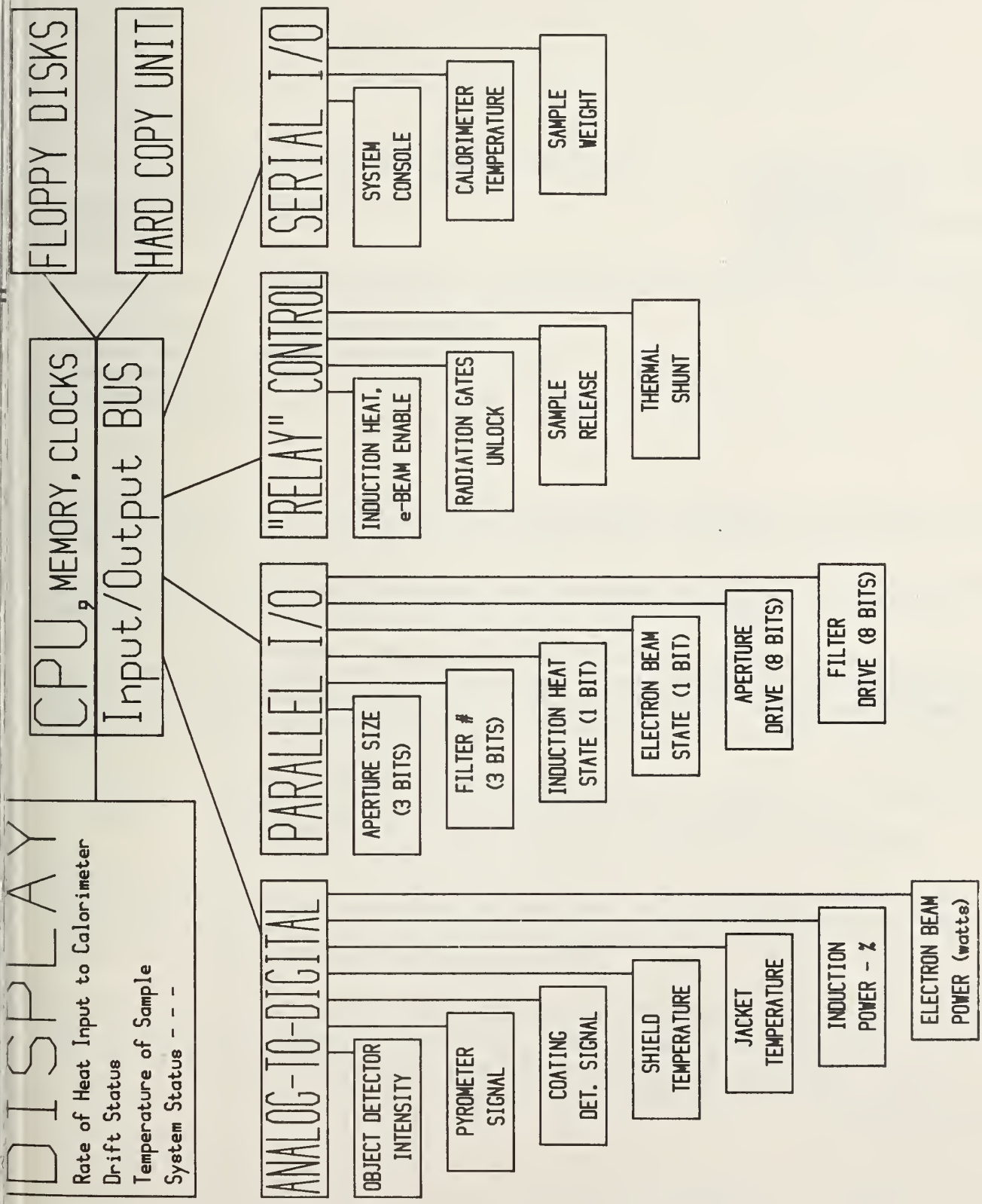
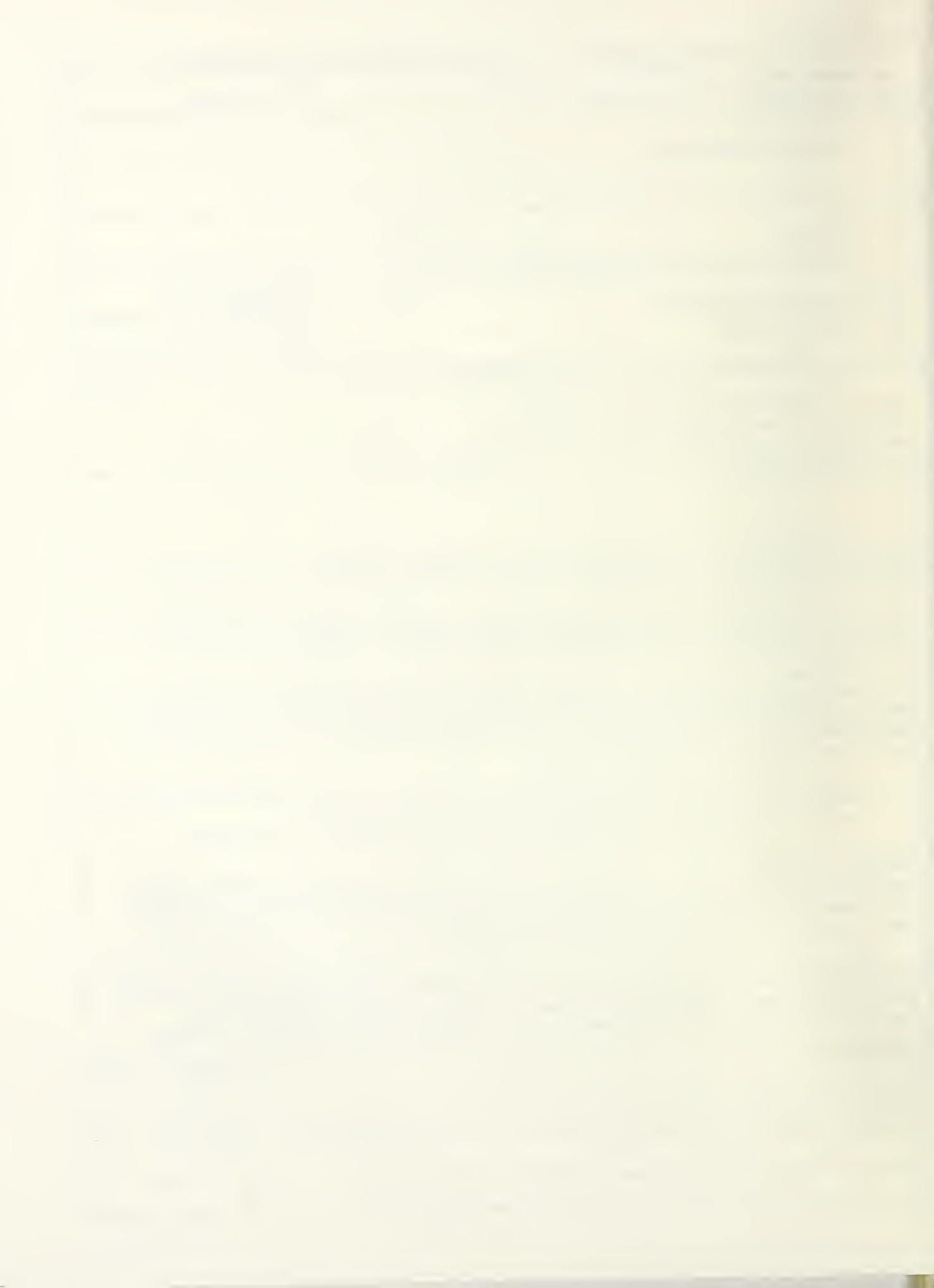


Fig. 2. Block diagram of automation system with a detailed breakdown of the necessary input/output structure.



U.S. DEPT. OF COMM. <b>BIBLIOGRAPHIC DATA SHEET</b> (See instructions)		1. PUBLICATION OR REPORT NO. NBSIR 82-2560	2. Performing Organ. Report No.	3. Publication Date July 1982
4. TITLE AND SUBTITLE NBS: Materials Measurements				
5. AUTHOR(S) J. R. Manning				
6. PERFORMING ORGANIZATION (If joint or other than NBS, see instructions) NATIONAL BUREAU OF STANDARDS DEPARTMENT OF COMMERCE WASHINGTON, D.C. 20234			7. Contract/Grant No. NASA Gov't Order H - 27954 B	8. Type of Report & Period Covered Annual Report April 1, 1981 - Mar. 31,
9. SPONSORING ORGANIZATION NAME AND COMPLETE ADDRESS (Street, City, State, ZIP) Office of Materials Processing in Space National Aeronautics and Space Administration Washington, D. C. 20546				1982
10. SUPPLEMENTARY NOTES  <input type="checkbox"/> Document describes a computer program; SF-185, FIPS Software Summary, is attached.				
11. ABSTRACT (A 200-word or less factual summary of most significant information. If document includes a significant bibliography or literature survey, mention it here) <p>This report describes NBS work for NASA in support of NASA's Materials Processing in Space Program under NASA Government Order H-27954B (Properties of Electronic Materials) covering the period April 1, 1981 to March 31, 1982.</p> <p>This work is directed toward measurement of materials properties important to the design and interpretation of space processing experiments and investigations of how the space environment may offer a unique opportunity for performing improved measurements and producing materials with improved properties. This work is being carried out in three independent tasks:</p> <ul style="list-style-type: none"><li>Task 1. Surface Tensions and Their Variations with Temperature and Impurities</li><li>Task 2. Convection during Unidirectional Solidification</li><li>Task 3. Measurement of the High Temperature Thermophysical Properties of Tungsten Group Liquids and Solids</li></ul> <p>Emphasis in Tasks 1 and 2 is on how the reduced gravity obtained in space flight can affect convection and solidification processes. Emphasis on Task 3 is toward development of techniques for thermodynamic measurements on reactive materials, requiring levitation and containerless processing.</p>				
12. KEY WORDS (Six to twelve entries; alphabetical order; capitalize only proper names; and separate key words by semicolons) Auger spectroscopy; convection; gallium-tin alloys; levitation calorimetry; segregation; specific heat; surface tension; thermophysical properties; tungsten.				
13. AVAILABILITY <input checked="" type="checkbox"/> Unlimited <input type="checkbox"/> For Official Distribution. Do Not Release to NTIS <input type="checkbox"/> Order From Superintendent of Documents, U.S. Government Printing Office, Washington, D.C. 20402. <input checked="" type="checkbox"/> Order From National Technical Information Service (NTIS), Springfield, VA. 22161			14. NO. OF PRINTED PAGES 104	15. Price \$12.00



The first part of the document discusses the importance of maintaining accurate records of all transactions. It emphasizes that every entry, no matter how small, should be recorded to ensure the integrity of the financial statements. This includes not only sales and purchases but also expenses and income. The document provides a detailed list of items that should be tracked, such as inventory levels, accounts payable, and accounts receivable. It also outlines the procedures for reconciling these accounts and identifying any discrepancies.

The second part of the document focuses on the classification of expenses. It explains how different types of costs should be categorized based on their nature and purpose. For example, direct materials and labor costs are classified as manufacturing costs, while overhead expenses are treated as indirect costs. The document provides a clear framework for allocating these costs to the appropriate cost centers and then to the final products. This process is essential for determining the true cost of production and for setting competitive prices.

The third part of the document addresses the issue of depreciation. It discusses the various methods used to calculate the value of fixed assets over their useful lives. The straight-line method is the most common, but other methods like the declining balance and the sum-of-the-years-digits method are also mentioned. The document explains how depreciation affects the financial statements and the tax liability of the company. It also provides a table showing the calculation of depreciation for different assets and methods.

The fourth part of the document deals with the preparation of financial statements. It outlines the steps involved in creating the income statement, balance sheet, and cash flow statement. It emphasizes the importance of consistency and accuracy in these reports, as they provide a clear picture of the company's financial performance and position. The document also discusses the role of auditors in verifying the accuracy of these statements and the consequences of misstatements.

Finally, the document concludes with a summary of the key points discussed. It reiterates the importance of thorough record-keeping, proper classification of costs, and accurate calculation of depreciation. It also stresses the need for transparency and honesty in financial reporting, as this is the foundation of trust and success in any business.

